Machine Learning for Reservoir Quality Prediction in Chlorite-Bearing Sandstone Reservoirs

Nichols, Thomas E.; Worden, Richard H.; Houghton, James E.; Griffiths, Joshua; Brostrøm, Christian; Martinius, Allard W.

DOI
10.3390/geosciences15080325

Publication date
2025

Document Version
Final published version

Published in
Geosciences (Switzerland)

geosciences

MDPI

Article

Machine Learning for Reservoir Quality Prediction in Chlorite-Bearing Sandstone Reservoirs

Thomas E. Nichols [1], Richard H. Worden [1,*], James E. Houghton [1], Joshua Griffiths [1,2], Christian Brostrøm [3] and Allard W. Martinius [3,4]

[1] Diagenesis Research Group, Department of Earth, Ocean, and Ecological Sciences, School of Environmental Sciences, University of Liverpool, 4 Brownlow Street, Liverpool L69 3GP, UK
[2] United Kingdom National Nuclear Laboratory, 5th Floor, Chadwick House, Birchwood Park, Risley, Warrington WA3 6AE, UK
[3] Equinor ASA, Arkitekt Ebbells veg 10, N-7053 Ranheim, Norway; awma@equinor.com or a.w.martinius@tudelft.nl (A.W.M.)
[4] Faculty of Civil Engineering and Geosciences, Technical University of Delft, Stevinweg 1, 2628 CN Delft, The Netherlands
* Correspondence: r.worden@liverpool.ac.uk

Abstract

We have developed a generalisable machine learning framework for reservoir quality prediction in deeply buried clastic systems. Applied to the Lower Jurassic deltaic sandstones of the Tilje Formation (Halten Terrace, North Sea), the approach integrates sedimentological facies modelling with mineralogical and petrophysical prediction in a single workflow. Using supervised Extreme Gradient Boosting (XGBoost) models, we classify reservoir facies, predict permeability directly from standard wireline log parameters and estimate the abundance of porosity-preserving grain coating chlorite (gamma ray, neutron porosity, caliper, photoelectric effect, bulk density, compressional and shear sonic, and deep resistivity). Model development and evaluation employed stratified K-fold cross-validation to preserve facies proportions and mineralogical variability across folds, supporting robust performance assessment and testing generalisability across a geologically heterogeneous dataset. Core description, point count petrography, and core plug analyses were used for ground truthing. The models distinguish chlorite-associated facies with up to 80% accuracy and estimate permeability with a mean absolute error of 0.782 log(mD), improving substantially on conventional regression-based approaches. The models also enable prediction, for the first time using wireline logs, grain-coating chlorite abundance with a mean absolute error of 1.79% (range 0–16%). The framework takes advantage of diagnostic petrophysical responses associated with chlorite and high porosity, yielding geologically consistent and interpretable results. It addresses persistent challenges in characterising thinly bedded, heterogeneous intervals beyond the resolution of traditional methods and is transferable to other clastic reservoirs, including those considered for carbon storage and geothermal applications. The workflow supports cost-effective, high-confidence subsurface characterisation and contributes a flexible methodology for future work at the interface of geoscience and machine learning.

Keywords: machine learning; grain-coating chlorite; porosity-preservation; permeability; lithofacies; heterolithic sandstones; wireline logs; extreme gradient boosting; deltaic sandstone; clay-mineral

Academic Editor: Meng Lu

Received: 17 April 2025
Revised: 5 August 2025
Accepted: 11 August 2025
Published: 19 August 2025

Citation: Nichols, T.E.; Worden, R.H.; Houghton, J.E.; Griffiths, J.; Brostrøm, C.; Martinius, A.W. Machine Learning for Reservoir Quality Prediction in Chlorite-Bearing Sandstone Reservoirs. *Geosciences* **2025**, *15*, 325. https://doi.org/10.3390/geosciences15080325

1. Introduction

The mineral chlorite is an important constituent of many clastic sedimentary rocks, as it can have a significant impact (both positive and negative) on hydrocarbon field reservoir quality (porosity and permeability), as a function of its abundance and morphology. Chlorite can occur in the sedimentary environment as detrital grains, or develop in the diagenetic realm by the transformation of a precursor mineral such as smectite, kaolinite, or berthierine (an Fe-rich clay) to form authigenic chlorite [1–5]. Present in moderate quantities, chlorite can preserve porosity by forming grain coats that serve to inhibit quartz cementation by acting as a barrier between a detrital grain and silica-rich pore fluid, which might otherwise precipitate quartz on the quartz substrate during meso-diagenesis (>80 °C) [4,6–8]. The absence of chlorite may allow extensive quartz cementation to occur, degrading reservoir quality. A sandstone may contain too much chlorite so as to fill pores and block pore throats, reducing permeability just as extensive quartz cementation would. Therefore, a 'Goldilocks zone' sweet spot of chlorite content (not too little but not too much) must be present in the rock to mitigate negative effects and maximise porosity preservation [9]. Chlorite grain coats have been reported to form in sediments from almost every clastic sedimentary environment in a variety of basins [1,10]. Indeed, they are responsible for elevated porosity at depth (>3 km) in a large number of oil and gas fields globally [5,11,12] such as the Ordos Basin in China [13,14], the Gulf of Mexico [12], and the North Sea [15–20]. Therefore, advancing our understanding of the origin and improving the prediction of the distribution of grain-coating chlorite in sandstones is crucial for reservoir appraisal and development in chlorite-rich intervals found across the world.

The Lower Jurassic siliciclastic Tilje Formation in the Halten Terrace area of the North Sea (Figure 1) hosts elevated porosity compared to regional porosity-depth trends [19,20]. In fields such as Smørbukk, the enhanced porosity observed in this formation has been attributed mainly to the formation of continuous chlorite grain coats on the surface of detrital quartz grains before the onset of quartz cementation [20–22]. In the Tilje Formation, Fe-rich minerals in lithic fragments and Fe-rich clays in ooids, possibly sourced from hypersaline lagoons, have been reported to contribute to the formation of authigenic chlorite coats [18]. However, the distribution of chlorite grain coats within the Tilje Formation is not uniform, and varies on a bed-scale due to the heterolithic nature and variable depositional controls on its occurrence, but has been found to be facies-controlled by core-based studies [18,23,24]. These challenges, which are not unique to the Tilje, mean that predicting chlorite grain coat distribution vertically and laterally on a large scale is difficult, even with traditional methods such as petrophysical interpretation of wireline logs, or seismic data [25,26].

Petrophysical data obtained by wireline are ubiquitous in the energy industry due to their utility to characterise sediment attributes and distinguish reservoir from non-reservoir [27]. In basic cases, this is achieved using a gamma ray log, which has high responses in many mudstones (typically considered low permeability) due to K-, Th-, or U-bearing clay minerals and low response in many sandstones (typically considered higher permeability) due to the absence of clay minerals [27,28]. However, petrophysical discrimination of chlorite is complex as it theoretically contains no radioactive elements to contribute to a gamma ray response, and has a high neutron response and low resistivity, both of which can be affected by pore fluid [4,29]. Typically, a core-based study is required to understand the distribution of chlorite within an interval of one well; however, this is expensive and spatially limited. Being able to understand the occurrence of chlorite within a field using wireline petrophysical data would allow for a highly novel, cheap, high-resolution field-wide interpretation of chlorite grain coat distribution.

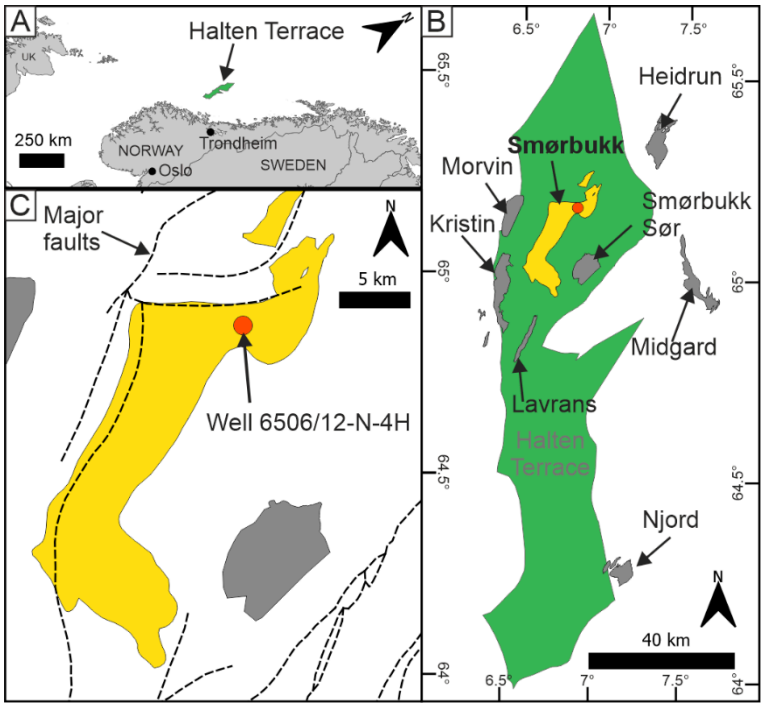

Figure 1. (**A**) Location of the Halten Terrace offshore mid-Norway. (**B**) Producing hydrocarbon fields within the Halten Terrace area. (**C**) Position of well 6506/12-N-4H within the Smørbukk field investigated in this study. Dashed lines represent major faults (data obtained from the Norwegian Offshore Directorate https://www.sodir.no/en/about-us/open-data/, accessed on 17 August 2023; modified after [18]).

Machine learning is the use of computational methods to identify patterns in data without being explicitly programmed, typically with the intention of creating robust predictive models for application to unknown samples [30]. In the context of oil and gas exploration, machine learning has been utilised to aid reservoir quality prediction in a variety of geological settings, employing different data types [31–34]. Supervised machine learning algorithms train models to classify samples with a known continuous (e.g., chlorite abundance, porosity) or discrete classification label (e.g., facies, lithology) using associated data as predictors (e.g., wireline) [35–38]. Wireline log data have been used as predictors for diagenetic facies or lithology, or to directly predict reservoir properties in machine learning models [33,34,39], and could be adapted to predict chlorite grain coat abundance. The present study contributes to the growing literature on the use of machine learning methods for lithofacies and permeability prediction in hydrocarbon exploration and reservoir characterisation, with the addition of grain coating chlorite quantification, which is key to understanding many reservoirs [40–44]. The ability of machine learning methods to outperform conventional methods for predicting reservoir quality parameters, and their ability to provide additional geological information, such as lithofacies, highlights the advantages of machine learning use over other statistical methods [39,45].

This study is designed to test the highly novel ability of a supervised machine learning algorithm to predict the occurrence of porosity-preserving grain coating chlorite in a deeply-buried reservoir qualitatively with a model predicting lithofacies, and quantitatively with a separate model predicting petrographic data, and to identify what factors affect performance. A third model quantitatively predicts permeability (calibrated using conventional core analysis). All the models created use petrophysical wireline data as predictors, thus enabling a rapid method of determining the presence of chlorite grain coats in a well without the need for additional core. We have trained models using data obtained from the deeply-buried (to 4.2 km TVD) heterolithic Tilje Formation in well 6506/12-N-4H

of the North Sea. Before training the three separate predictive machine learning models, we used a statistical approach to establish how predictor wireline log variables relate to porosity, permeability, lithofacies, and the abundance and morphology of chlorite. Then, machine learning models were trained to predict lithofacies distribution (in a classification model), and grain-coating chlorite abundance and permeability (in regression models). The performance of each model has been analysed, highlighting where predictions are accurate and where they are inaccurate, quantifying the importance of each predictor petrophysical variable in reducing model error to enhance interpretations. Ultimately, we have identified and synthesised possible sedimentological, petrophysical, and engineering influences on model performance to discuss more broadly how machine learning may be used as a tool to make predictions in chlorite-rich clastic petroleum reservoirs.

2. Geological Setting

2.1. Tilje Formation, Smørbukk Field

The Halten Terrace area of the Norwegian North Sea contains several fields which produce hydrocarbons from the Tilje Formation (Figure 1) [23,24,46]. The Tilje Formation, part of the Båt Group, is a highly heterolithic and heterogeneous sequence of tide-dominated deltaic and shallow to marginal marine sandstones, as well as associated siltstones and mudstones that were deposited during the Early Jurassic (Figure 2) [18,24,47]. Sedimentation during this time was locally controlled by the formation of the Halten Basin during the Late Triassic-Early Jurassic early syn-rift phase of the opening of the North Atlantic Ocean [47,48]. Local variations in subsidence, sediment supply, and depositional processes give rise to multi-scale heterogeneities in the type and extent (spatial and temporal) of primary depositional facies, which are further compounded by early to late burial diagenetic processes [23,24,46,49].

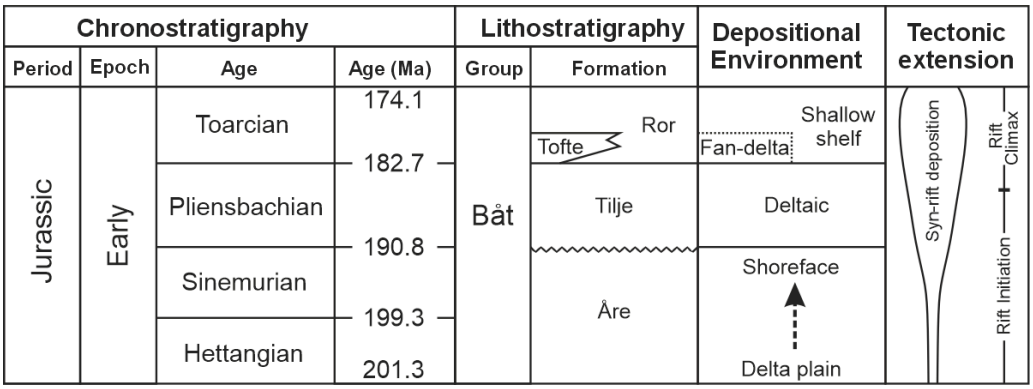

Figure 2. Summary of the Early Jurassic lithostratigraphy in the Halten Terrace area indicating approximate depositional environment and tectonic activity. The present study focuses on the top of the Tilje Formation in well 6506/12-N-4H (modified after [47]).

Lithological heterogeneity within the formation, and the distribution of depositional facies introduce challenges for hydrocarbon exploration, field appraisal and development, as well as production; however, improvements in reservoir characterisation and prediction have improved recovery [24]. Across the formation at shallow to moderate depths (<3.5 km burial), reservoir quality may be controlled by sediment texture (grain size and sorting), overpressure, or calcite cementation [24]. However, in deeper fields (>3.5 km burial) such as Kristin, Smørbukk Sør, and Smørbukk (the focus of this study), the presence and total grain coverage of grain coating chlorite is the principal control on reservoir quality [18,20,23,24]. Therefore, in such fields, understanding the distribution of

grain-coating and pore-filling chlorite and the facies that contain them is crucial to reducing uncertainty during reservoir development.

2.2. Sedimentology and Reservoir Quality Controls in Well 6506/12-N-4H of the Smørbukk Field

Core 6506/12-N-4H is a production well drilled in the Smørbukk field of the Norwegian North Sea in the year 2000. The well was drilled in 272 m water depth down to a measured depth (mRKB) of 6212 m and true vertical depth (mTVD) of 4922 m, terminating in the Late Triassic Åre Formation that underlies the Tilje Formation (Figure 2). Non-continuous core was recovered from the well between 5610 and 6122 mRKB. The well is deviated, and bedding has an apparent dip of 50° relative to the horizontal of the core. The focus of the present study is on three cored reservoir sections of Tilje Formation in well 6506/12-N-4H between 4263 and 4216 mTVD (Figure 1). The reservoir intervals are as follows: Section 1 between 5974 and 5986 mRKB, Section 2 between 5939 and 5956 mRKB, and Section 3 between 5893 and 5907 mRKB. These three intervals have been subjected to high-resolution targeted sampling by Griffiths, Worden, Utley, Brostrøm, Martinius, Lawan and Al-Hajri [18], for analysis by petrographic point-counting, X-ray diffraction for mineral identification and quantification, and facies description. The study reconstructed the paleoenvironmental conditions during deposition, but crucially determined the major controls on reservoir quality and the origin of grain-coating and pore-filling chlorite.

Griffiths et al. [18] reported that the three described reservoir intervals constituted three different facies associations: tidal channel (FA1), tidal-fluvial channel (FA2), and distributary mouth bar (FA3) (Figure 3A). The three facies associations were made up of eight lithofacies, which were further split into fourteen sub-facies, distinguished by variations in bioturbation type and intensity (after [50]), grain size, sedimentary structures, and bedding style (Table 1). Within well 6506/12-N-4H, the intervals characterised are interpreted to represent a shift from being tidally-dominated (reservoir Section 1), to mixed tidal-fluvial (reservoir Section 2), to fluvially-dominated (reservoir Section 3) as a result of variability in seasonal rainfall, autogenic lobe switching, eustatic sea-level change, and tectonically-generated accommodation space (Figure 3) [18,49,51].

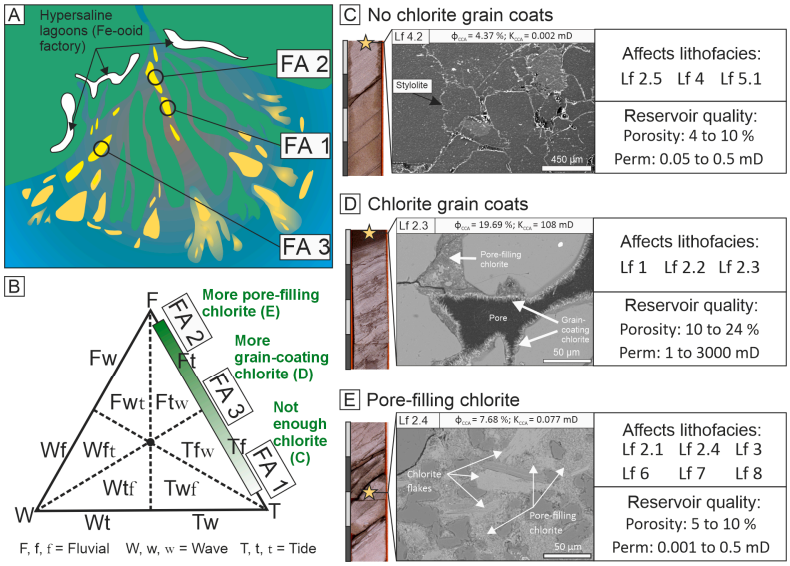

Figure 3. Summary of depositional environment model and reservoir quality controls at the top of the Tilje Formation of well 6506/12-N-4H. (**A**) Interpreted depositional environment for facies associations 1 to 3 present within the reservoir sections in this study (modified after [49]). (**B**) Interpreted processes active during deposition of facies associations (FA) 1 to 3 and the relation of those processes to chlorite grain coat occurrence (modified after [51]). (**C**) Representative SEM image of 5982 mRKB showing the effects of no chlorite grain coats on reservoir quality, where quartz cementation has not

been inhibited. (**D**) Representative SEM image of 5895 mRKB showing chlorite as coats on the surface of detrital quartz grains, leading to preserved porosity at depth by the inhibition of quartz cement. (**E**) Representative SEM image of 5939.5 mRKB showing the effects of too much chlorite as a pore-filling matrix, blocking pores (modified after [18,46]).

Table 1. Summary of the lithofacies scheme used to describe the three reservoir sections investigated in this study, with interpreted controls on reservoir quality. For lithofacies classification, sub-facies 2.2 and 2.3 are merged into 'Lf2.2_3', separate from sub-facies 2.1, 2.4, and 2.5, which form 'Lf2.1_4_5', and lithofacies 7 and 8 are merged into the class 'Lf7_8'. Bioturbation index is defined after Taylor and Goldring [50]: 0—no bioturbation; 1—low bioturbation, bedding distinct, few discrete traces; 2—moderate bioturbation, low trace density; 3—high bioturbation, traces discrete, sharp bedding boundaries, rare overlap; 4—high bioturbation, indistinct bedding boundaries, high trace density with common overlap; 5—intense bioturbation, high trace density, completely disturbed bedding; 6—complete bioturbation, sediment reworked due to repeated overprinting (based on [47]).

Facies	Subfacies	Grain Size and Sedimentary Structures	Bioturbation Type and Intensity	Environmental Interpretation	Reservoir Quality Controls/Effect of Chlorite	Reservoir Quality Properties
Lf1: Cross-stratified sandstone with quartz pebbles	No subfacies (n = 32)	Medium- to coarse-grained, moderately well-sorted sandstone with sub-rounded quartz pebbles and granules. Individual beds have erosive basal contacts, often lined by quartz pebbles and/or granules.	BI: 0. Absent.	Tidal-fluvial channel bar close to the tidal limit.	Positive. Chlorite grain coats (5–15% gc chlorite) inhibit quartz cementation, preserving porosity and permeability	15–20% porosity, 100 s to 1000 s mD permeability.
Lf2: Cross-stratified heterolithic sandstones	2.1: Cross-stratified sandstone with fluid mud (n = 7)	Medium-grained and moderately-sorted cross-stratified sandstone with homogeneous fluid mud layers (<2 cm) at basal contacts. Fluid mud layers become less frequent upward (in younger deposits), and grain size typically increases	BI: 0. Absent.	Tidal-fluvial channel bar at or close to the central turbidity maximum.	Negative. Pore-filling chlorite decreases porosity and permeability	~11% porosity, ~10 mD permeability
	2.2: Cross-stratified sandstone with flasers (n = 24)	Medium- to coarse-grained, moderately well- to poorly-sorted, and relatively structureless sandstones, with localised isolated mud flasers, interbedded with silty-sandstone. Bed contacts can be bioturbated or erosional.	BI: 0 to 1 (locally 3 to 4). Absent to moderate. Small-scale *Skolithos*.	Tidal-fluvial channel point-bar.	Positive. Grain-coating chlorite inhibits quartz cementation, preserving porosity and permeability	10 to 15% porosity, 10 to 1000 mD permeability
	2.3: Bioturbated cross-stratified sandstone (n = 36)	Medium-grained, moderately-sorted, and intensely bioturbated cross-stratified interbedded with bioturbated silty-sandstone. Basal contacts can be sharp, erosional, gradational, and bioturbated. Bed thickness and grain size typically increase upwards.	BI: 2 to 4. Low to high. Small-scale mixed *Cruziana-Skolithos* bioturbation assemblages	Distributary mouth bar.	Positive. Grain-coating chlorite inhibits quartz cementation, preserving porosity and permeability	10 to 25% porosity
	2.4: Trough cross-stratified sandstone with fluid mud and/or conglomeratic lag (n = 7)	Coarse-grained and poorly-sorted trough cross-stratified sandstone. Erosional basal contacts are lined by fluid mud (<2 cm) and quartz granules and pebbles.	BI: 0. Absent.	Tidal-fluvial dunes at or close to the central turbidity maximum.	Negative. Pore-filling	~7% porosity
	2.5: Speckled sandstone with fluid mud (n = 12)	Medium-grain and moderately sorted cross-stratified sandstone with single and compound fluid mud layers (<2 cm). Bioturbated and fragmented mud layers (mud intraclasts) give the sandstone a speckled appearance.	BI: 1 to 4. Sparse to intense. Small-scale *Skolithos*.	Fluvial-influenced tidal-channel bar.	Negative. Pore-filling	5 to 10% porosity

Table 1. *Cont.*

Facies	Subfacies	Grain Size and Sedimentary Structures	Bioturbation Type and Intensity	Environmental Interpretation	Reservoir Quality Controls/Effect of Chlorite	Reservoir Quality Properties
Lf 3: Current rippled and cross-laminated sandstone	No subfacies (n = 25)	Fine-grained, well- to moderately-sorted, current rippled, cross-laminated sandstone. Current-ripple laminar sets are bound by double mud drapes and flow-reversal structures.		Tidal-channel bar with slow-moving currents	Negative. Pore-filling	~12% porosity
Lf4: Cross-stratified sandstone with sand-mud couplets	4.1: Cross-stratified sandstone with sporadic sand-mud couplets (n = 26)	Medium- to coarse-grained sandstone with an abundance of sand-mud couplets.	BI: 0. Absent.	Confined tidal dune top-sets. Sand-mud couplets are preferentially eroded on the top sets of tidal dunes.	No chlorite. Quartz cementation allowed to occur unhindered, blocking pores.	~8% porosity
	4.2: Laminae-sets of sand-mud couplets	Medium- to coarse-grained sandstone with an abundance of sand-mud couplets.	BI: 0. Absent.	Confined tidal dune toe-sets. Sand-mud couplets are preferentially preserved in the toe-sets of dunes.	No chlorite. Quartz cementation allowed to occur unhindered, blocking pores.	5 to 8% porosity
Lf5: Sandstones with large-scale *Diplocraterion*	5.1: Cross-stratified sandstone with large-scale *Diplocraterion* (n = 19)	Medium- to coarse-grained, moderately- to poorly-sorted sandstone with faint to clear cross-stratification and/or current ripple cross-lamination with double mud drapes. Local iron staining is present.	BI: 2 to 5. Low to intense. Small-scale *Skolithos* and large-scale *Diplocraterion* and *Teichichnus*.	Tidal-channel bar margin or point-bar (periodic fluvial influence).	No chlorite. Quartz cementation allowed to occur unhindered.	~8% porosity
	5.2: Homogenised sandstone with large-scale *Diplocraterion*	Medium- to coarse-grained, moderately- to poorly-sorted sandstone with barely visible cross-stratification, ripple cross-lamination, and local double mud drapes, due to intense bioturbation.	BI: 5 to 6. Intense to completely bioturbated. Small-scale *Skolithos* and large-scale *Diplocraterion* and *Teichichnus*.		Negative. Pore-filling chlorite and quartz cement	~8% porosity
Lf 6: Intensely bioturbated heterolithics	6.1: Bioturbated sand-dominated heterolithics (60:40 to 90:10 sand/mud) (n = 70)	Fine-grained, well- to moderately-sorted sandstone with barely visible current-rippled cross-lamination due to intense bioturbation.	BI: 5 to 6 (mostly 6). Intense to completely bioturbated. High-diversity. Small-scale *Planolites*, *Skolithos*, and less common large-scale *Diplocraterion*.	Tidal-channel bar margin or point-bar.	Negative. Pore-filling chlorite and quartz cement	11% porosity
	6.2: Bioturbated mixed sand/mud heterolithics (40:60 to 60:40 sand/mud)	Very fine- to medium-grain, poorly- to moderately-sorted, bioturbated sand-dominated heterolithics with locally preserved current ripple cross-lamination, flaser and lenticular bedding.	BI: 3 to 5. Moderate to intense. High diversity. *Planolites*, *Skolithos*, *Diplocraterion*, *Teichichnus*, and *Chondrites*.	Sub-aqueous tidal flat.	Negative. Pore-filling chlorite and quartz cement	5 to 10% porosity
	6.3: Bioturbated mud-dominated heterolithics (10:90 to 40:60 sand/mud) (n = 1)	Very fine- to fine-grained, poorly- to moderately-sorted, bioturbated mixed sand and mud heterolithics with locally preserved current rippled cross-lamination.	BI: 3 to 6. Moderate to intense. High diversity. *Planolites*, *Skolithos*, *Diplocraterion*, *Teichichnus*, and *Chondrites*.		Negative. Pore-filling chlorite and quartz cement	5 to 10% porosity
Lf7: Wavy-bedded sand-dominated heterolithics showing current-ripple cross lamination	No subfacies (n = 6)	Wavy-bedded fine-grained, moderately well-sorted, sandstone with ripple cross-lamination bound by homogeneous and laminated mud layers (0.5 to 3 cm thick).	BI: 0 to 1. Absent to sparse. Small-scale *Diplocraterion* in sand intervals. Small-scale *Planolites* in laminated and lenticular-bedded mudstone layers.	Tidal-fluvial channel.	Negative. Pore-filling chlorite.	<5% porosity
Lf 8: Lenticular-bedded ripple cross-laminated sandstone	8.1: Bioturbated lenticular-bedded ripple cross-laminated sandstone (n = 17)	Intensely bioturbated, very fine- to fine-grained, poorly sorted, with locally preserved ripple cross-laminated and lenticular bedding.	BI: 3 to 5. Low to high. *Skolithos*, *Diplocratrion*, *Planolites*, *Paleophycus*, *Cyclindrichnus*, and *Chondrites*.	Tidal-flival channel margin or point-bar top.	No chlorite. Poorly sorted with minimal cements, main porosity loss attributed to mechanical compaction.	<5% porosity
	8.2: Non-bioturbated lenticular-bedded ripple cross-laminated sandstone	Very fine- to fine-grained, poorly-sorted, sandstone with clear current-ripple cross-lamination and lenticular bedding.	BI: 0. Absent.		RQ controlled by texture? Too mud-rich?	<5% porosity

The study concluded that reservoir quality was primarily controlled by the presence, absence, and total volume of grain-coating chlorite and pore-filling chlorite, which in turn

controlled the extent of quartz cement [18]. Grain-coating chlorite, sourced from iron-rich precursor lithics and iron ooids, locally preserves reservoir quality by inhibiting quartz cementation (Figure 3D), whereas pore-filling chlorite occludes pore space and blocks pore throats (Figure 3E), significantly reducing porosity and permeability. Where grain-coating or pore-filling chlorite is not present, extensive quartz cementation has destroyed porosity. Chlorite grain coats are effectively absent from the tidal channel facies association (FA1) but are present in the tidal-fluvial channel (FA2) and distributary mouth bar (FA3) facies associations; however, FA2 is also likely to contain pore-filling chlorite, reducing porosity (Figure 3). FA2 and FA3 are contrasting sedimentologically as FA2 contains metre-scale massive coarse-grained sandstone beds (Lf1) with minor muddy facies (e.g., Lf7, Lf8), whereas FA3 is highly heterolithic, containing interbedded bioturbated cross-stratified sandstone (Lf2.3) and mixed bioturbated sand-mud heterolithics (Lf6). The strong facies-controlled nature of chlorite grain coat distribution in this well provides a strong basis to use it as a proxy to predict reservoir quality using supervised machine learning classification.

3. Materials and Methods

3.1. Core 6506/12-N-4H Wireline, Lithofacies Description, and Petrographic Point-Count Data

In the following section, we will outline the wireline log parameters used as predictor data, core analysis data, lithofacies description, and chlorite grain coat abundance used as labels to be predicted by three separate models. In addition, we will provide details of statistical analyses carried out on the data, and finally describe the machine learning workflow that we have employed. Lithofacies and petrographic point count data presented and used in this study were originally generated by Griffiths et al. [18].

3.1.1. Predictor Features: Wireline Log Data

Wireline data used in this study were obtained via the Norwegian Offshore Directorate (previously Norwegian Petroleum Directorate). The data were obtained at a measurement spacing of 0.1524 m (6 inches) with an 8.5-inch drill bit for the length of the entire section analysed in this study. Eight wireline parameters were employed to train models: neutron porosity (NPHI; %), photoelectric effect (PEF; unitless), caliper (CALI; inches), compressional wave delay time (DTCO; µs/ft), shear wave delay time (DTS; µs/ft), bulk density (RHOB; gcm^{-3}), gamma ray (GR; API), and deep resistivity (RD; Ωm). All of these parameters act as the predictor variables in training data to predict horizontal core analysis permeability in regression 'Model C', lithofacies in classification 'Model A', and point-counted grain-coating chlorite in regression 'Model E'. A summary of predictor features and training labels is presented in Table 2.

Table 2. Summary of wireline data used as predictor features and training labels for Model A, Model C, and Model E.

	Predictor Features								Training Labels		
	Neutron Porosity (Fraction)	**Photoelectric Factor (P_e)**	**Caliper (in)**	**Compressional Wave Delay (µs/ft)**	**Shear Wave Delay (µs/ft)**	**Bulk Density (gcm^{-3})**	**Gamma Ray (API)**	**Deep Resistivity (Ωm)**	**Model C: Core Analysis Permeability (mD)**	**Model E: Point Count Grain-Coating Chlorite (%)**	**Model A: Litho-facies**
Count	282	282	282	282	282	282	282	282	163	54	282
Mean	0.09284	4.1336	8.676	69.57	118.87	2.499	51.69	13.66	109.167	4.55	-
Std. dev	0.0347	1.3061	0.223	5.281	9.212	0.102	20.73	4.25	418.478	4.99	-
Min	0.01275	0.3965	8.34	61.08	94.52	2.214	28.47	5.99	0.000	0.00	-
Lower Quartile	0.07169	3.2505	8.517	65.72	112.67	2.437	35.78	11.39	0.002	0.00	-
Median	0.0969	3.7549	8.625	68.37	116.79	2.512	43.55	13.06	0.015	2.50	-
Upper Quartile	0.1168	4.5581	8.753	72.43	125.37	2.563	63.86	15.38	0.276	8.70	-
Max.	0.17326	10.4839	9.293	85.2	146.38	2.739	123.5	26.58	3086.169	16.30	-

3.1.2. Model C Training Labels: Conventional Core Analysis Permeability

Core plugs were taken from core 6506/12-N-4H by the operator Equinor to carry out conventional core analysis (CCA), measuring porosity (as a fraction) and permeability (in

milliDarcys, mD). Within the three reservoir sections investigated in this study, there are 195 measurements of porosity (φ_{CCA}) and 163 measurements of horizontal permeability (K_{CCA}). The core analysis horizontal permeability measurements were selected to be used as label variables in Model C. We did not choose to model porosity using machine learning, as this can be done with reasonable accuracy using a conventional standard bulk density (RHOB) transformation, which produces an R^2 score of 0.733.

Prior to model training and testing, permeability values were transformed using the $\log_{10}(x)$, where x is permeability (mD), as it was found to solve problems in model predictions. Using raw permeability measurements as an objective in some cases led to negative permeability predictions, which is physically impossible. It was also found that the model trained on raw data performed well at predicting permeability values >100 mD but very poorly at permeability values <100 mD, likely due to the linear nature of the selected objective metric, root mean square error (rmse), meaning it is unsuitable for measuring the error of a variable that spans many orders of magnitude, such as permeability.

3.1.3. Model A Training Labels: Lithofacies Description

The objective of the lithofacies classification Model A is to distinguish, based on wireline parameters, the lithofacies that contain enough grain-coating chlorite to preserve reservoir quality, namely lithofacies 1 and sub-lithofacies 2.2 and 2.3, from non-reservoir lithofacies intervals (Table 1; Figure 3). Intervals coincident with wireline log data in Tilje Formation reservoir units, Sections 1–3, have been labelled according to the lithofacies scheme as proposed by Griffiths et al. [18] (Table 1). In total, 282 core intervals have been manually assigned lithofacies labels, forming the training label dataset for classification Model A.

Here we have trained a model to classify lithofacies, rather than facies association or sub-facies (Table 1). The sub-facies within lithofacies 2, Lf 2.1, 2.4, and 2.5 have been merged to form class 'Lf2.1_4_5', separated from Lf 2.2 and 2.3, which form the class 'Lf2.2_3'. We have separated these sub-facies as even though they belong to the same over-arching lithofacies, they are reported to have very different reservoir quality, attributed to grain-coating chlorite present in Lf 2.2 and Lf 2.3, which has preserved porosity and permeability, while Lf 2.1, 2.4, and 2.5 host pore-filling chlorite, reducing reservoir quality [18]. Lithofacies 7 (n = 6) and 8 (n = 17) have been merged to form the 'Lf7_8' class to increase sample size for the class and, as they both have poor reservoir quality due to pore-filling chlorite, suit the intended utility of the model.

3.1.4. Model E Training Labels: Petrographic Point Count Grain-Coating Chlorite

Point counted grain coating chlorite (PCGCC) was chosen as the regression objective in Model E, as it is the main control on reservoir quality in the studied reservoir sections [18]. Training labels for this model were generated by Griffiths et al. [18] from the optical point counting of 300 grains in polished thin sections taken from horizontal core plugs. In total, 54 thin sections were point counted (14 in reservoir Section 1, 20 in reservoir Section 2, and 20 in reservoir Section 3) and contributed to the training set for Model E. Prior to model training, raw values of PCGCC (in percent) were transformed using $\log_{10}$ to force non-negativity of predictions. A total of 20 of 54 PCGCC values were measured as zero. In order to preserve zero values of PCGCC after log-transformation, zero values were artificially set to 0.1%; previously, the lowest non-zero value was 0.3%. Table 2 summarises raw PCGCC data.

3.2. Statistical Analyses

To investigate the relationships between wireline log parameters, core analysis data, and lithofacies, we have carried out statistical tests on the combined dataset. First, the Pearson's correlation coefficient (R) has been determined to describe the strength of the

relationships between wireline log parameters, PCGCC, and core analysis porosity (fractional) and horizontal permeability ($\log_{10}$(mD)), with corresponding *p*-values for each test quantifying the significance of each relationship. In addition, an analysis of variance (ANOVA) test was carried out to assess whether there are statistically significant differences in wireline log parameters as a function of lithofacies. Following the ANOVA test, a post-hoc Tukey's honest significant difference (HSD) test determined which lithofacies were statistically significantly different from one another as a function of wireline log parameters. All statistical analyses were performed in RStudio version 4.3.0 [52].

3.3. Machine Learning Workflow

3.3.1. Overview

In this study, we present predictive machine learning regression models, which predict continuous variables, and a classification model that predicts a discrete class-based variable. To train predictive machine learning models, we have opted to use the supervised decision tree-based Extreme Gradient Boosting (XGBoost) algorithm in RStudio [52,53] available through the 'xgboost' package and tools within the 'tidymodels' package for hyperparameter optimisation [54,55]. XGBoost was chosen as some studies show that it is able to outperform other algorithms, specifically in geophysical prediction models [56,57]. The workflow employed to train models has been adapted from Houghton, Nichols, Griffiths, Simon, Utley, Duller and Worden [38] and Nichols, Worden, Houghton, Duller, Griffiths and Utley [37] who predicted the sub-depositional environment and estuarine zone in a modern estuary using bulk sediment grain size characteristics and geochemistry. The workflow has been adapted here to use wireline log data obtained from well 6506/12-N-4H as predictors for permeability regression (Model C), lithofacies classification (Model A), and point-counted grain-coating chlorite regression (Model E) as outlined in previous sections. Regression models C and E used the evaluation metric RMSE (Table 3) as the objective metric to minimise during hyperparameter optimisation, and model training and testing.

Table 3. Evaluation Metrics for classification and regression models used in this study. TN = True negative, FN = False negative, TP = True positive, FP = False positive (modified after [35,58]).

Model Type	Metric Name	Equation	Description
Classification (Model A)	Precision	$\frac{TP}{TP+FP}$	The proportion of positive predictions that are true positives versus false positives
	Recall	$\frac{TP}{TP+FN}$	The rate at which a classifier identifies true positive labels versus to false negatives
	F1	$\frac{TP}{TP+\frac{1}{2}(FP+FN)}$	A measure of accuracy combining precision and recall, which does not take into account true negatives
	Overall Accuracy	$\frac{\sum_{i=1}^{l}\frac{TP_i+TN_i}{TP_i+TN_i+FP_i+FN_i}}{l}$	Overall effectiveness of a classifier at identifying true labels, where 'l' is the number of classes
Regression (Model C and E)	Root mean square error (RMSE)	$\sqrt{\frac{\sum_{i=1}^{N}(x_i-\hat{x}_i)^2}{N}}$	A metric scaled to the predicted label dataset; a lower score indicates greater accuracy.
	Coefficient of determination (R^2)	$1-\frac{\sum_{i=1}^{N}(x_i-\hat{x}_i)^2}{\sum_{i=1}^{N}(x_i-\overline{x})^2}$	A score ranging from 0 to 1, where 0 indicates no correlation between actual values and predicted values and 1 indicates perfect agreement between actual and predicted values.
	Mean absolute error (MAE)	$\frac{\sum_{i=1}^{N}\lvert x_i-\hat{x}_i\rvert}{N}$	Mean of the absolute error between actual and predicted values; lower score indicates higher accuracy

The machine learning workflow employed to create predictive models is outlined in Figure 4. The workflow is split into the following three sections:

(1) Importing of wireline log and point counting data with lithofacies labels;
(2) Bayesian optimisation of XGBoost hyperparameters;
(3) Model training and testing with 4-fold partitioning.

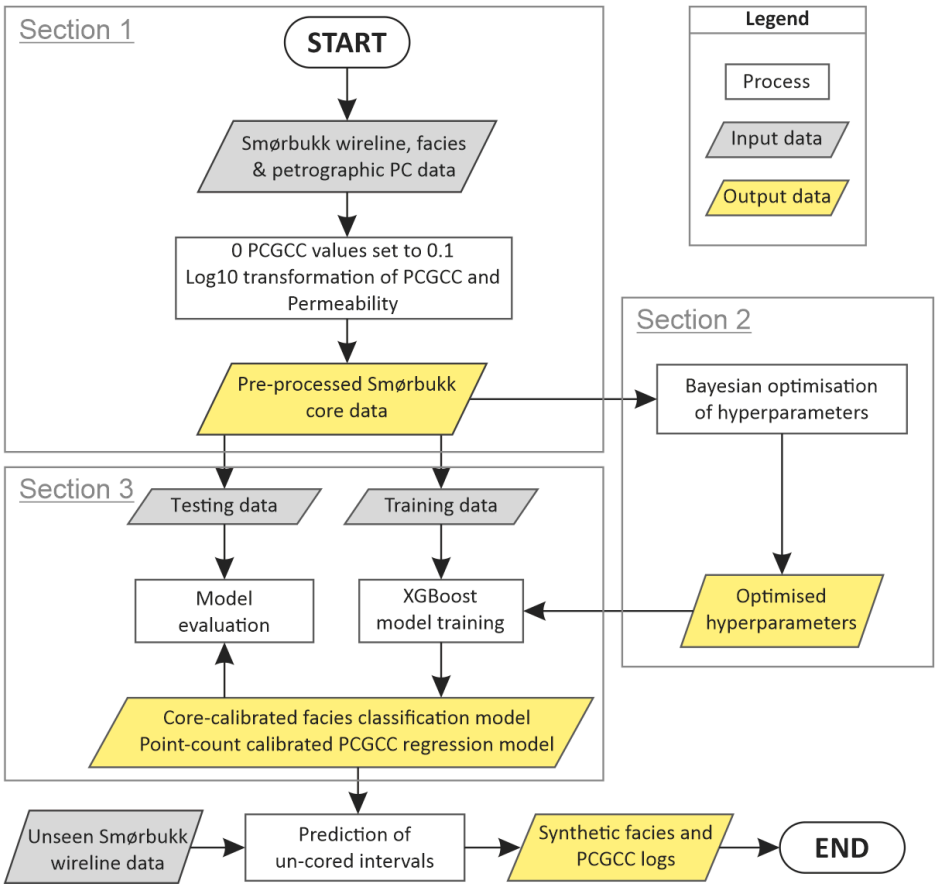

Figure 4. Diagram illustrating the machine learning workflow employed in this study.

Hyperparameters are adjustable numerical values that control how a machine learning model is built to improve performance and control over-fitting. For example, hyperparameters can set the maximum number of splits allowed in a decision tree or force sub-sampling of predictor variables or training samples. Default hyperparameter values may not be suitable for all datasets or classification problems, and, if untuned, can lead to unrepresentatively poor model performance. Therefore, it is necessary to find the optimum values suitable for each training/testing dataset [59]. Within the model creation workflow, hyperparameters are selected by Bayesian optimisation (BO) and k-fold cross-validation (after [38,59]). The BO process evaluates the performance of models made using different combinations of hyperparameters spread evenly across the hyperparameter space selected by Latin hypercube sampling within search ranges set by the user. For all models created in this study, we have optimised the following hyperparameters (with the search ranges in parentheses): nrounds (10 to 1000); max_depth (4 to 30); min_child_weight (1 to 10); gamma (−1 to 3); subsample (0.6 to 1); colsample_bytree (2 to 7); eta (−3 to −1).

Once a model has been trained using Extreme Gradient Boosting, the 'importance' of each predictor variable (known as a feature) used in model training can be extracted. The importance score of all features sums to one and indicates what proportion of training error is reduced by each feature, where the higher the score, the more important that feature is for reducing error in the model.

3.3.2. Model Evaluation and Comparison

In order to evaluate the performance of individual lithofacies within the classification Model A, we have employed the evaluation metrics: recall, precision, and F1 score. These metrics provide information about aspects of model performance, such as proportion of

true positive predictions (precision), and overall effectiveness at identifying true positives and true negatives (overall accuracy) [35,58]; these are summarised in Table 3.

To evaluate the performance of regression Model C and E, we have employed the root mean square error (RMSE), the coefficient of determination (R^2), and mean absolute error (MAE), also summarised in Table 3 [60].

4. Results

4.1. Facies Analysis and Wireline Data

Raw wireline log data and petrographic point-count pore-filling and grain-coating chlorite data for the reservoir sections of well 6506/12-N-4H are presented in Figures 5–7 alongside a graphic sedimentary log. The three reservoir sections are highly heterogeneous in terms of grain size, bed thickness, sedimentary structures, and bioturbation type and intensity. A summary of wireline log parameters and core analysis properties is presented as a function of lithofacies in Figure 8.

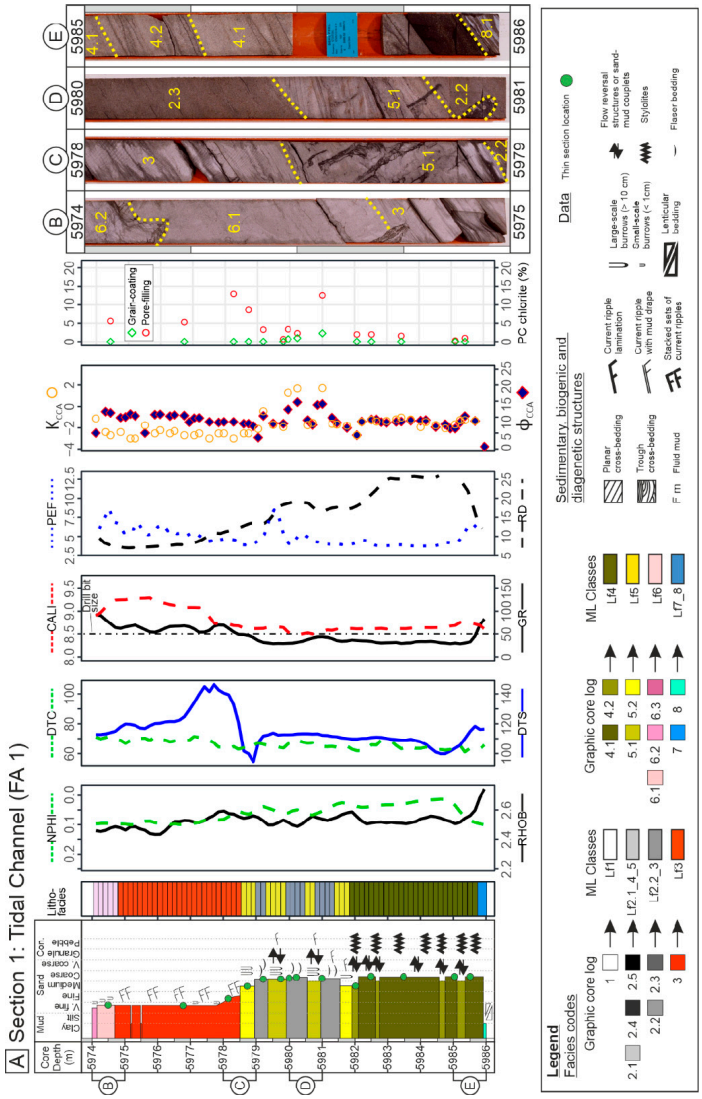

Figure 5. (**A**) Composite wireline log data of the tidal channel facies association (FA1) in well 6506/12-N-4H with graphic sedimentary log, conventional core analysis porosity (φ_{CCA}) and permeability (K_{CCA}), and petrographic point count data for grain coating (green diamonds) and pore-filling (red circles) chlorite abundance. Core photographs of: (**B**) 5974 to 5975 mRKB; (**C**) 5978 to 5979 mRKB; (**D**) 5980 to 5981 mRKB; and (**E**) 5985 to 5986 mRKB showing each of the lithofacies in this reservoir section.

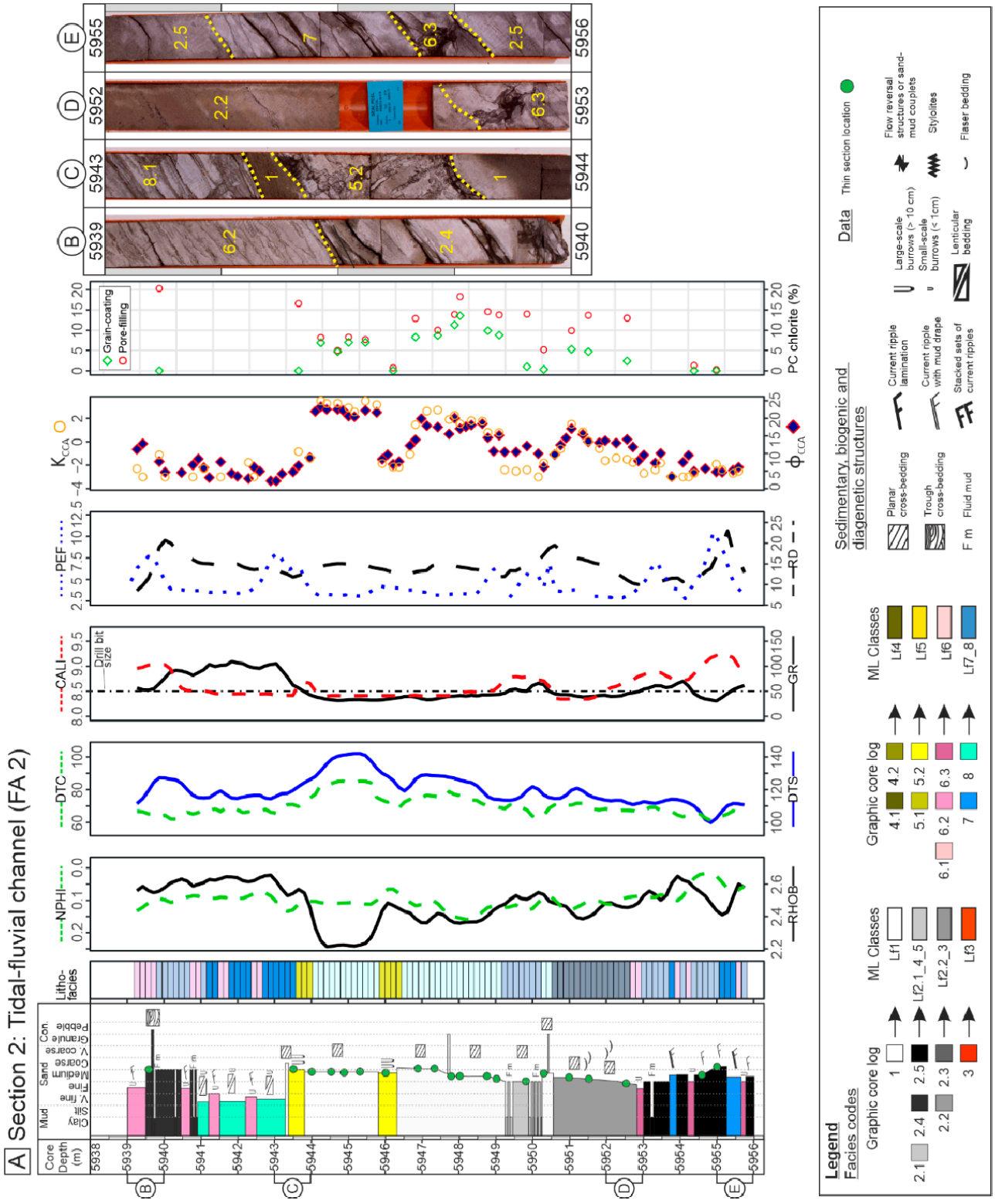

Figure 6. (**A**) Composite wireline log data of the tidal-fluvial channel facies association (FA2) in well 6506/12-N-4H with graphic sedimentary log, conventional core analysis porosity (φ_{CCA}) and permeability (K_{CCA}), and petrographic point count data for grain coating (green diamonds) and pore-filling (red circles) chlorite abundance. Core photographs of: (**B**) 5939 to 5940 mRKB; (**C**) 5943 to 5944 mRKB; (**D**) 5952 to 5953 mRKB; and (**E**) 5955 to 5956 mRKB, illustrating the lithofacies diversity in the reservoir section.

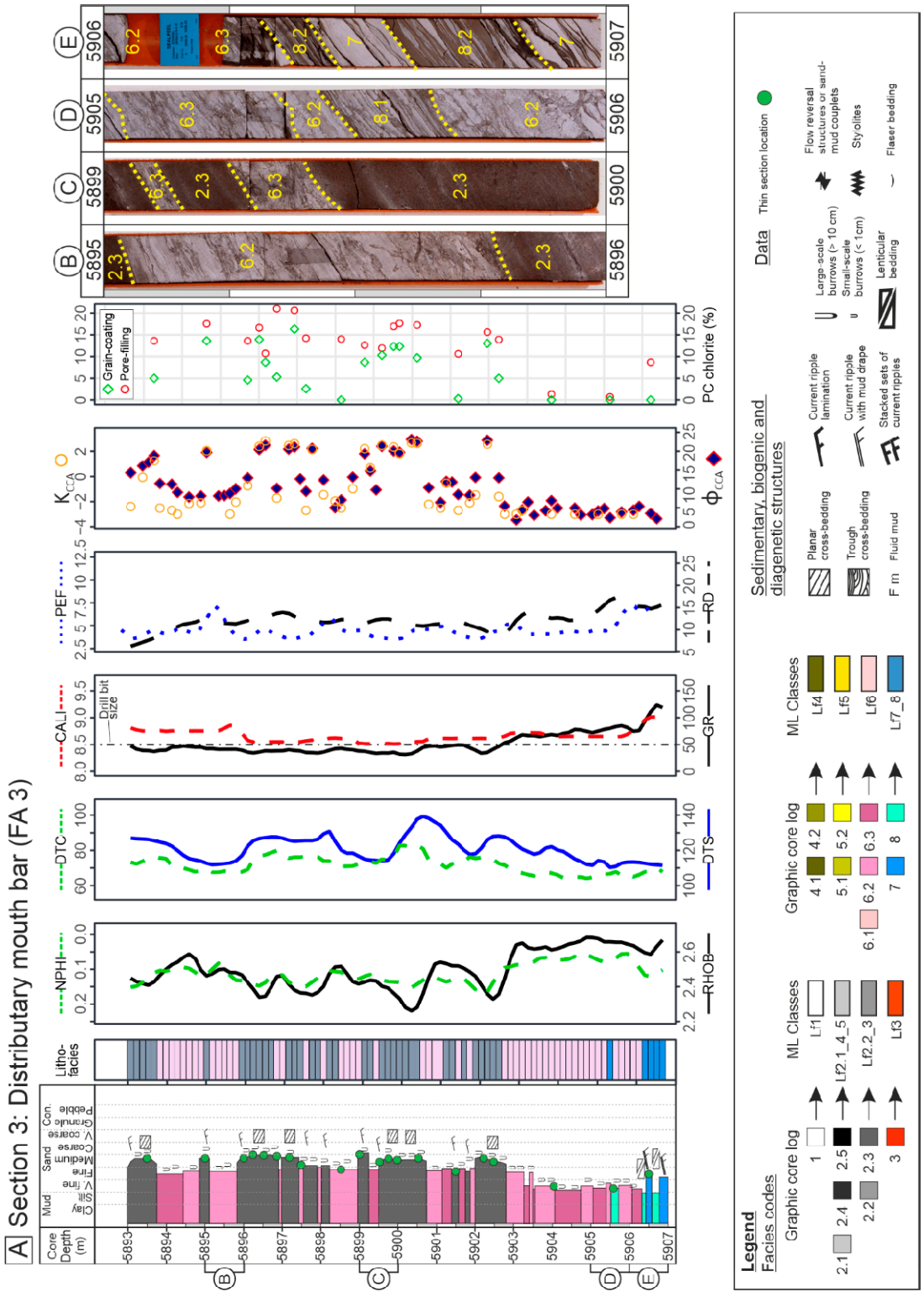

Figure 7. (**A**) Composite wireline log data of the distributary mouth bar facies association (FA3) in well 6506/12-N-4H with graphic sedimentary log, conventional core analysis porosity (φ_{CCA}) and permeability (K_{CCA}), and petrographic point count data for grain coating (green diamonds) and pore-filling (red circles) chlorite abundance. Core photographs of: (**B**) 5895 to 5896 mRKB; (**C**) 5899 to 5900 mRKB; (**D**) 5905 to 5906 mRKB; and (**E**) 5906 to 5907 mRKB showing the highly heterolithic and interbedded nature of this reservoir section.

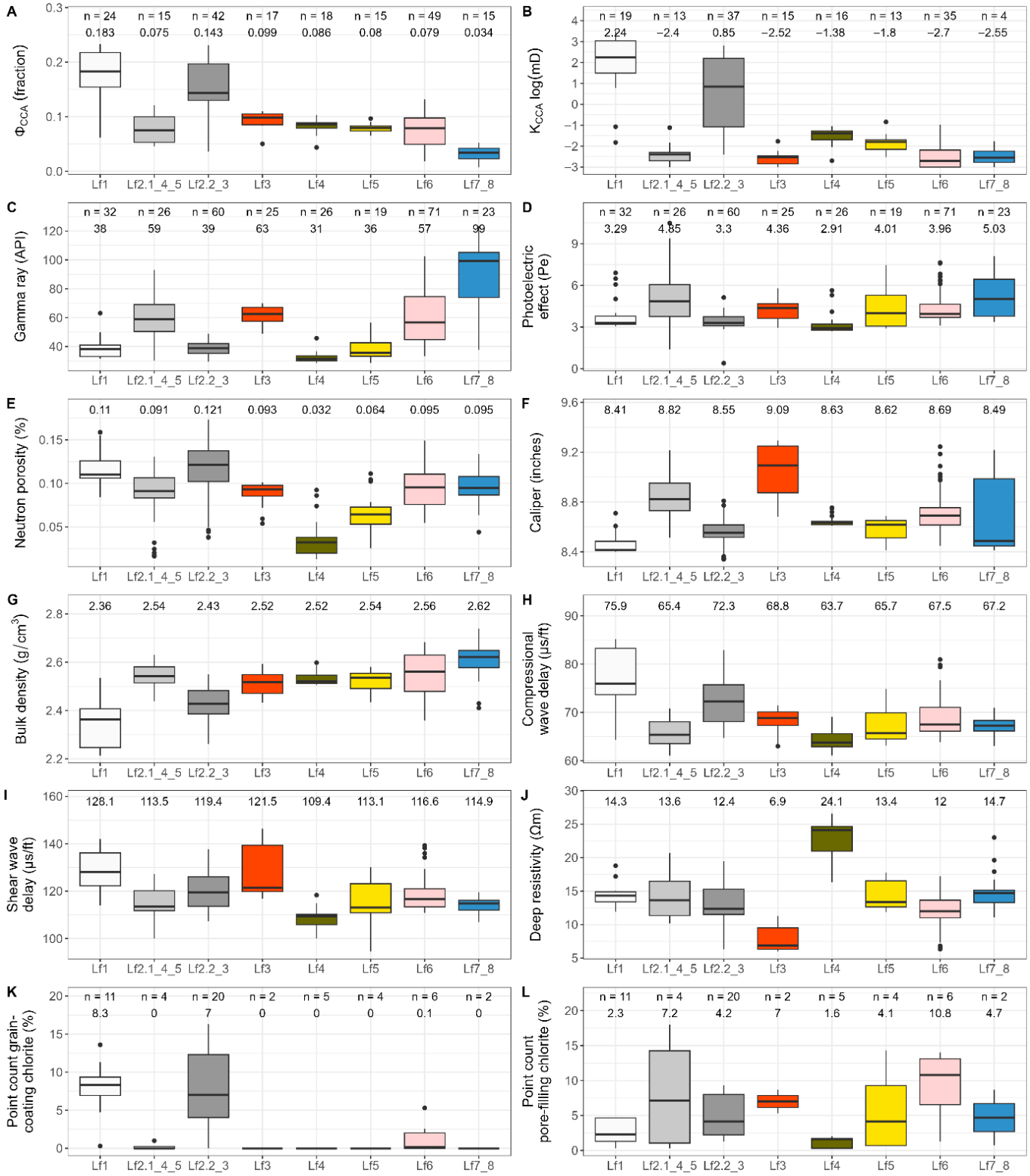

Figure 8. Boxplots of core analysis properties, (**A**) porosity, (**B**) log-permeability, wireline parameters: (**C**) Gamma ray; (**D**) Photoelectric effect; (**E**) Neutron porosity; (**F**) Caliper; (**G**) Bulk density; (**H**) Compressional wave delay; (**I**) Shear wave delay; (**J**) Deep resistivity. Petrographic point count abundance of (**K**) grain-coating chlorite, and (**L**) total chlorite as a function of lithofacies. Numbers at the top of each sub-plot are sample numbers (*n* = x) and the median values of each parameter for each lithofacies. Sample numbers for sub-plots C to J are the same.

In the tidal channel facies association (FA1; Figure 5), elevated tidal energy conditions have winnowed fines and deposited coarse clean sands which contain neither pore-filling

nor grain-coating chlorite, particularly in lithofacies 3 and 4. The result is reduced porosity and permeability caused by extensive quartz cementation and stylolitisation in the top and bottom of the section (Table 1; Figure 3C; Figure 5). Beds of lithofacies 2.2 occur in the middle of this section, hosting low amounts of chlorite grain coats, resulting in moderate reservoir quality beds between beds of poor quality Lf5.

The tidal-fluvial channel facies association (FA2; Figure 6) is highly heterogeneous, containing thin beds (0.2 to 0.8 m) of non-reservoir lithofacies 2.1, 2.4, 2.5, 5, 6, 7, 8, which host pore-filling chlorite due to the mud-rich nature of the sediments (Table 1; Figure 3E). Reservoir Section 3 hosts lithofacies 1 and 2.2 as thick beds (2 to 4 m), which have marked increases in grain-coating chlorite, leading to elevated porosity and permeability compared to other facies (Figure 3).

The mixed tidal-fluvial distributary mouth bar facies association (FA3; Figure 7) contains lithofacies 2 interbedded with lithofacies 6 with bed thicknesses varying between 0.05 and 1.1 m. Lithofacies 2.2 and 2.3 contain grain-coating chlorite, which preserves reservoir quality (Table 1; Figure 3D). Pore-filling chlorite is present in this facies association in lithofacies 6 (Table 1; Figure 3E).

4.2. Statistical Analysis of Wireline and Core Analysis Data

Pearson's correlation coefficients have been derived to describe the statistical relationships between the continuous variables of wireline log parameters (e.g., neutron porosity, caliper, bulk density, etc.), core analysis measurements (porosity and permeability), and point-counted grain-coating chlorite (Table 4, Figure 8). Analysis of variance (ANOVA) reveals that there are statistically significant differences in some wireline log parameters between lithofacies classes. Results of the post-hoc Tukey Honestly Significant difference test are presented in Table 5, highlighting between which lithofacies there are significant differences ($p < 0.1$) in wireline log parameters.

Table 4. Pearson's correlation coefficient (R) matrix between wireline parameters and core analysis properties is shown in the bottom portion of the table, and *p*-values are shown in the top portion. Correlation coefficients are coded to show their statistical significance, where $p < 0.05$ is significant (*), $p < 0.01$ is very significant (**), $p < 0.001$ is extremely significant (***), and lighter shading indicates a more significant correlation.

	NPHI	PEF	CALI	DTCO	DTS	RHOB	GR	RD	log(K_{CCA})	φ_{CCA}	PCGCC
NPHI	1.000	0.815	0.009	0.0000	0.000	0.000	0.486	0.000	0.477	0.000	0.000
PEF	−0.014	1.000	0.000	0.000	0.007	0.000	0.000	0.002	0.010	0.000	0.025
CALI	−0.156 **	0.487 ***	1.000	0.000	0.003	0.000	0.000	0.000	0.000	0.000	0.001
DTCO	0.651 ***	−0.232 ***	−0.343 ***	1.000	0.000	0.000	0.000	0.000	0.000	0.000	0.000
DTS	0.541 ***	−0.161 **	−0.177 **	0.668 ***	1.000	0.000	0.374	0.000	0.000	0.000	0.003
RHOB	−0.457 ***	0.207 ***	0.230 ***	−0.795 ***	−0.465 ***	1.000	0.000	0.024	0.000	0.000	0.000
GR	0.042	0.292 ***	0.219 ***	−0.307 ***	−0.053	0.632 ***	1.000	0.001	0.000	0.000	0.020
RD	−0.517 ***	−0.180 **	−0.338 ***	−0.305 ***	−0.388 ***	0.135 *	−0.200 ***	1.000	0.203	0.048	0.030
log(K_{CCA})	0.405 ***	−0.296 ***	−0.533 ***	0.680 ***	0.350 ***	−0.778 ***	−0.508 ***	0.104	1.000	0.000	0.000
φ_{CCA}	0.527 ***	−0.332 ***	−0.309 ***	0.744 ***	0.481 ***	−0.856 ***	−0.555 ***	−0.142 *	0.881 ***	1.000	0.000
PCGCC	0.733 **	−0.305 *	−0.447 ***	0.656 ***	0.403 **	−0.692 ***	−0.317 *	−0.296 *	0.777 ***	0.828 ***	1.000

Table 5. ANOVA and post-hoc Tukey Honestly Significant Difference (HSD) test to identify which wireline parameters have statistically significant differences between lithofacies in well 6506/12-N-4H. *p*-values are coded to show their statistical significance, where $p < 0.1$ is marginally significant (+), $p < 0.05$ is significant (*), $p < 0.01$ is very significant (**), $p < 0.001$ is extremely significant (***), and lighter shading indicates a more significant difference.

Lithofacies Comparison			GR	RHOB	PEF	CALI	DTCO	DTS	RD	NPHI	PCGCC
2.1_4_5	vs.	1	0.000 ***	0.000 ***	0.000 ***	0.000 ***	0.000 ***	0.000 ***	1.000	0.000 ***	0.019 *
2.2_3	vs.	1	1.000	0.000 ***	0.914	0.064+	0.000 ***	0.000 ***	0.206	1.000	1.000
3	vs.	1	0.000 ***	0.000 ***	0.628	0.000 ***	0.000 ***	1.000	0.000 ***	0.002 **	0.126
4	vs.	1	0.735	0.000 ***	0.653	0.000 ***	0.000 ***	0.000 ***	0.000 ***	0.000 ***	0.006 **
5	vs.	1	1.000	0.000 ***	0.573	0.140	0.000 ***	0.000 ***	1.000	0.000 ***	0.014 *
6	vs.	1	0.000 ***	0.000 ***	0.130	0.000 ***	0.000 ***	0.000 ***	0.002 **	0.002 **	0.023 *
7_8	vs.	1	0.000 ***	0.000 ***	0.000 ***	0.000 ***	0.000 ***	0.000 ***	0.994	0.065+	0.126
2.2_3	vs.	2.1_4_5	0.000 ***	0.000 ***	0.000 ***	0.000 ***	0.000 ***	0.061+	0.348	0.000 ***	0.017 *
3	vs.	2.1_4_5	1.000	0.517	0.059+	0.000 ***	0.278	0.000 ***	0.000 ***	0.999	1.000
4	vs.	2.1_4_5	0.000 ***	0.990	0.000 ***	0.000 ***	0.938	0.016 *	0.000 ***	0.000 ***	1.000
5	vs.	2.1_4_5	0.000 ***	0.894	0.173	0.000 ***	0.793	1.000	1.000	0.117	1.000
6	vs.	2.1_4_5	1.000	1.000	0.029 *	0.016 *	0.006 **	0.540	0.008 **	0.744	1.000
7_8	vs.	2.1_4_5	0.000 ***	0.129	1.000	0.013 *	0.803	1.000	0.991	0.825	1.000
3	vs.	2.2_3	0.000 ***	0.000 ***	0.037 *	0.000 ***	0.000 ***	0.000 ***	0.000 ***	0.001 **	0.136
4	vs.	2.2_3	0.484	0.000 ***	0.993	0.246	0.000 ***	0.000 ***	0.000 ***	0.000 ***	0.004 **
5	vs.	2.2_3	1.000	0.000 ***	0.044 *	1.000	0.000 ***	0.117	0.306	0.000 ***	0.012 *
6	vs.	2.2_3	0.000 ***	0.000 ***	0.000 ***	0.000 ***	0.000 ***	0.814	0.646	0.000 ***	0.018 *
7_8	vs.	2.2_3	0.000 ***	0.000 ***	0.000 ***	0.043 *	0.000 ***	0.024 *	0.045 *	0.081+	0.136
4	vs.	3	0.000 ***	0.954	0.020 *	0.000 ***	0.012 *	0.000 ***	0.000 ***	0.000 ***	1.000
5	vs.	3	0.000 ***	1.000	1.000	0.000 ***	0.998	0.000 ***	0.000 ***	0.032 *	1.000
6	vs.	3	1.000	0.181	1.000	0.000 ***	0.991	0.000 ***	0.000 ***	0.982	1.000
7_8	vs.	3	0.000 ***	0.000 ***	0.050+	0.000 ***	0.994	0.000 ***	0.000 ***	0.983	1.000
5	vs.	4	0.849	0.999	0.022 *	0.825	0.157	0.046 *	0.000 ***	0.006 **	1.000
6	vs.	4	0.000 ***	0.923	0.000 ***	0.613	0.000 ***	0.000 ***	0.000 ***	0.000 ***	0.999
7_8	vs.	4	0.000 ***	0.012 *	0.000 ***	0.997	0.143	0.068+	0.000 ***	0.000 ***	1.000
6	vs.	5	0.000 ***	0.681	1.000	0.023 *	0.804	0.636	0.012 *	0.000 ***	1.000
7_8	vs.	5	0.000 ***	0.005 **	0.147	0.438	1.000	1.000	1.000	0.002 **	1.000
7_8	vs.	6	0.000 ***	0.054+	0.026 *	0.986	0.661	0.308	0.000 ***	1.000	1.000

4.3. Machine Learning Modelling Results

4.3.1. Model C: Permeability Regression

Model C was trained to predict horizontal core analysis permeability values within the core using all eight wireline log parameters as predictors (Table 2). The relative importance of each parameter in reducing error for Model C is shown in Figure 9. Bulk density (RHOB), caliper (CALI), and compressional wave delay (DTCO) are shown to be the three most important parameters with above-average contributions (>0.125), and all other parameters have below-average contributions (<0.125).

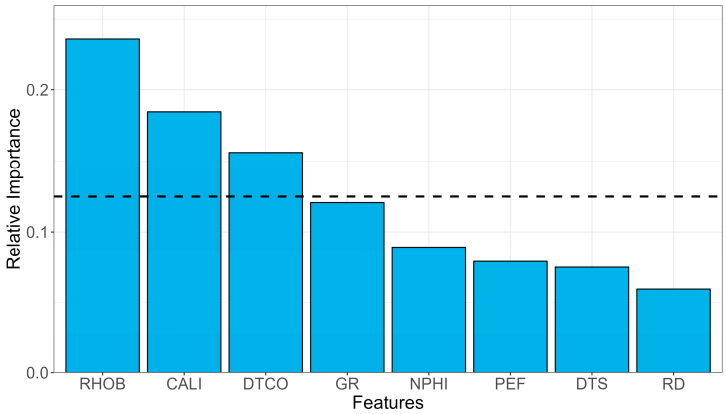

Figure 9. Relative importance of each wireline parameter in reducing error when training Model C. The bars above the dashed line represent variables that are above-average contributors to error reduction. (RD = deep resistivity; CALI = caliper; GR = gamma ray; RHOB = bulk density; NPHI = neutron porosity; PEF = photoelectric effect; DTS = shear wave delay; DTCO = compressional wave delay).

The amalgamated results of four folds of training/testing data are presented as a cross-plot of XGBoost prediction versus measured value in Figure 10. Performance metrics have been calculated on the log-transformed values of permeability so that the performance is not disproportionately impacted by the ability of the model to predict high permeability values compared to low ones. Across all four folds, R^2 score ranges between 0.6102 (fold 1) and 0.8865 (fold 4) but results in an amalgamated score of 0.6928, corresponding to a root mean square error (RMSE) of 1.09, and mean absolute error (MAE) of 0.782 (Table 6). However, these amalgamated scores may be skewed by the high performance of fold 4 (Table 6).

Figure 10 shows that 8 of 152 testing predictions lay outside a two orders of magnitude difference from the actual value; these occur in the lithofacies Lf2.2_3, Lf1, and Lf6. In order to investigate why these large errors have occurred, we present the results of Model C as a function of depth in the core in Figures 11D, 12D, and 13D, corresponding to reservoir Sections 1–3, respectively.

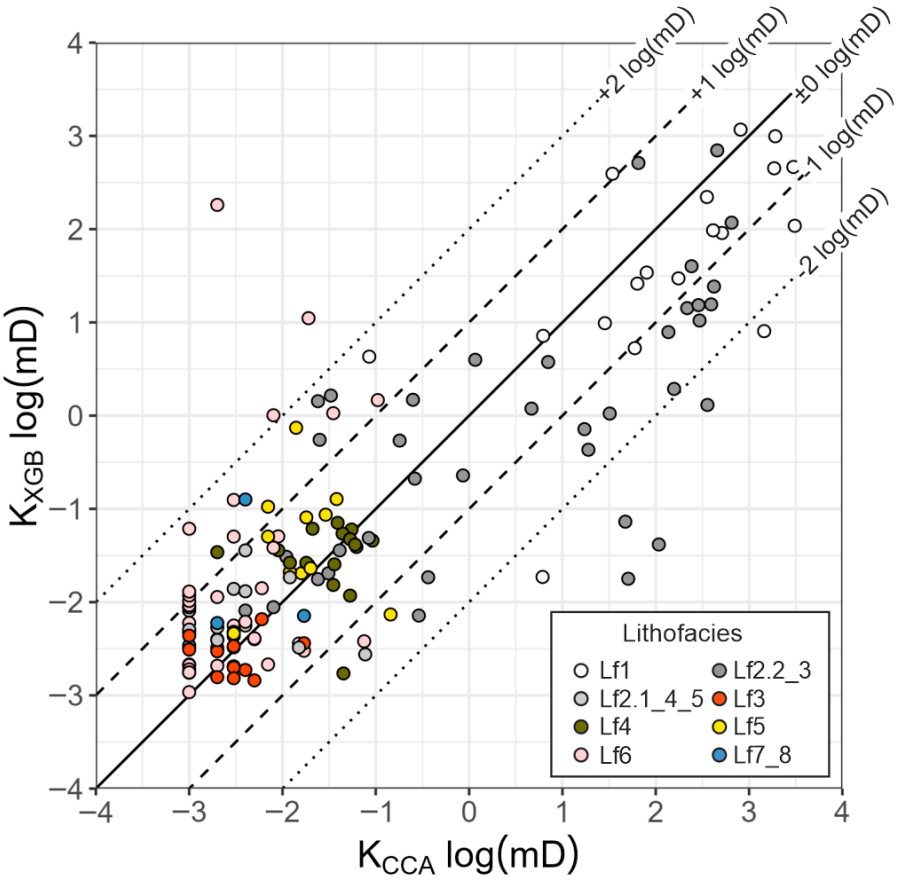

Figure 10. Cross-plot of XGBoost predicted core analysis permeability values (K_{XGB}) vs. measured values (K_{CCA}), shape-coded for the observed lithofacies of each sample.

Table 6. Evaluation metrics for individual folds of Model C testing data. See Table 3 for an explanation of evaluation metrics. These R^2 values can be compared to the prediction of permeability by linear regression of RHOB, for which R^2 = 0.605.

Fold	R^2	RMSE log(mD)	MAE log(mD)
1 (n_{test} = 38)	0.6102	1.10	0.808
2 (n_{test} = 38)	0.663	1.18	0.831
3 (n_{test} = 38)	0.6904	1.17	0.822
4 (n_{test} = 38)	0.8865	0.87	0.666
All (n_{test} = 152)	0.6928	1.09	0.782

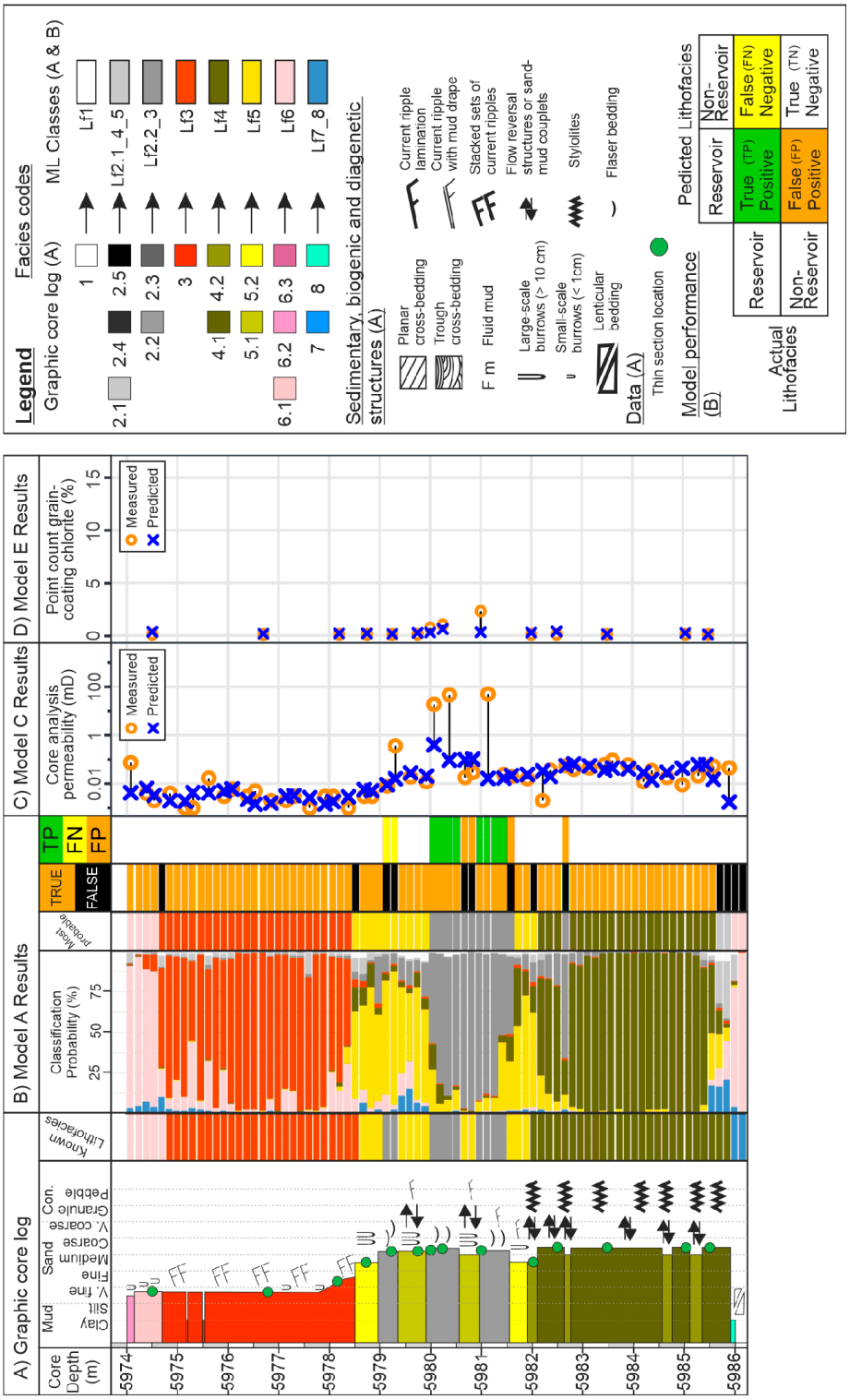

Figure 11. Lithofacies classification logs for reservoir Section 1 (Facies association 1) between 5974 and 5986 mRKB. Shown is (**A**) a graphic core log indicating grain size, the presence of sedimentary, biogenic, and diagenetic structures, and point-counted thin section samples alongside the assigned lithofacies label for each wireline measurement interval. (**B**) An amalgamation of test results for Model A showing the probability of a given lithofacies label for each interval; the most probable lithofacies label for that wireline interval; a log indicating whether the most probable lithofacies label assigned by the Model A is 'true' or 'false'; an indication of whether a prediction of Lf1 or Lf2.2_3 is a true positive (TP), false negative (FN) or false positive (FP). True negatives are left blank. (**C**) Amalgamated results of Model C core analysis permeability regression prediction. (**D**) Amalgamated results of Model E point count grain coating chlorite regression prediction.

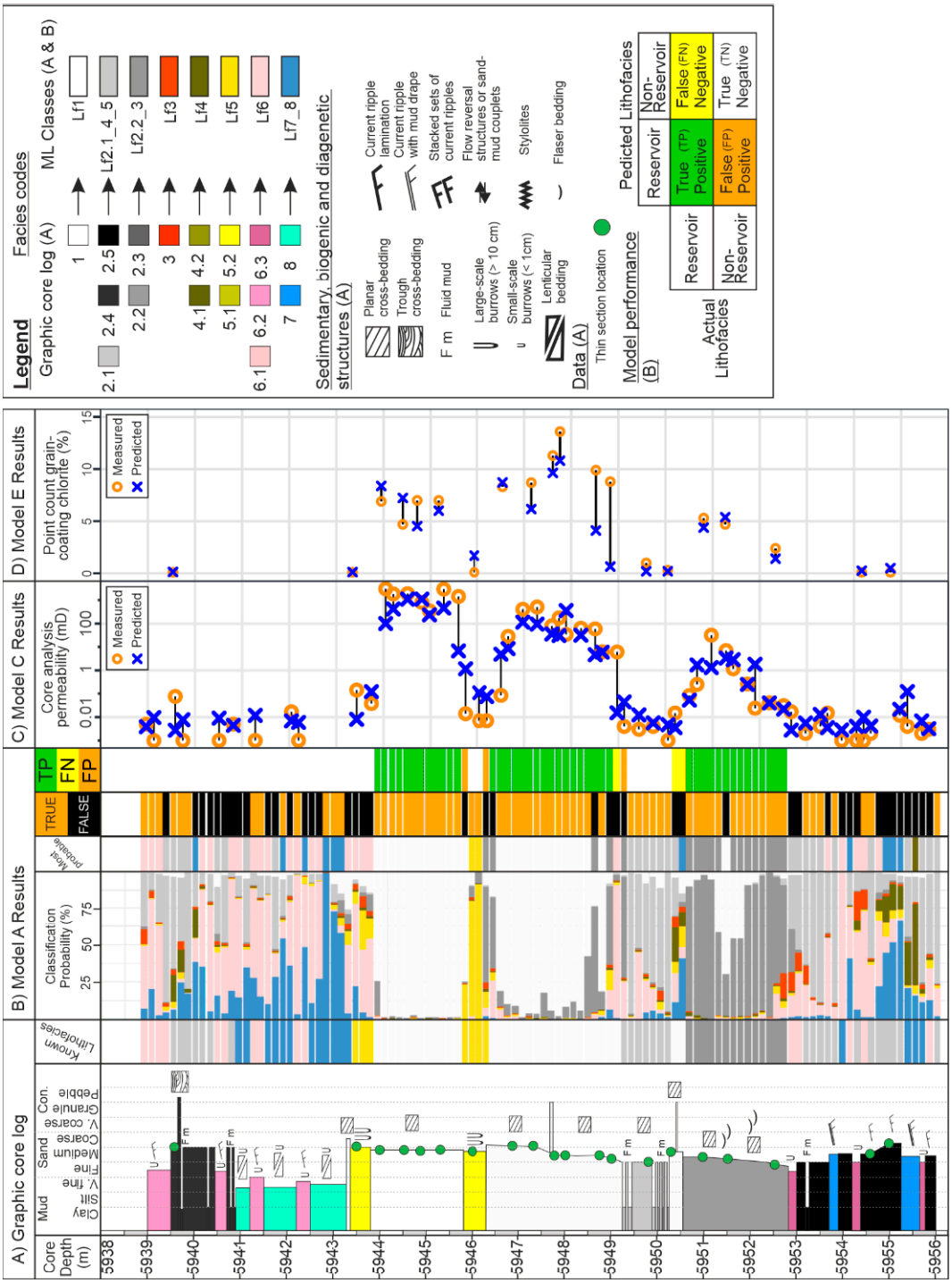

Figure 12. Lithofacies classification logs for reservoir Section 2 between 5942 and 5959 mRKB. Shown is (**A**) a graphic core log indicating grain size, the presence of sedimentary, biogenic, and diagenetic structures, and point-counted thin section samples alongside the assigned lithofacies label for each wireline measurement interval. (**B**) An amalgamation of test results for Model A showing the probability of a given lithofacies label for each interval; the most probable lithofacies label for that wireline interval; a log indicating whether the most probable lithofacies label assigned by the Model A is 'true' or 'false'; an indication of whether a prediction of Lf1 or Lf2.2_3 is a true positive (TP), false negative (FN) or false positive (FP). True negatives are left blank. (**C**) Amalgamated results of Model C core analysis permeability regression prediction. (**D**) Amalgamated results of Model E point count grain coating chlorite regression prediction.

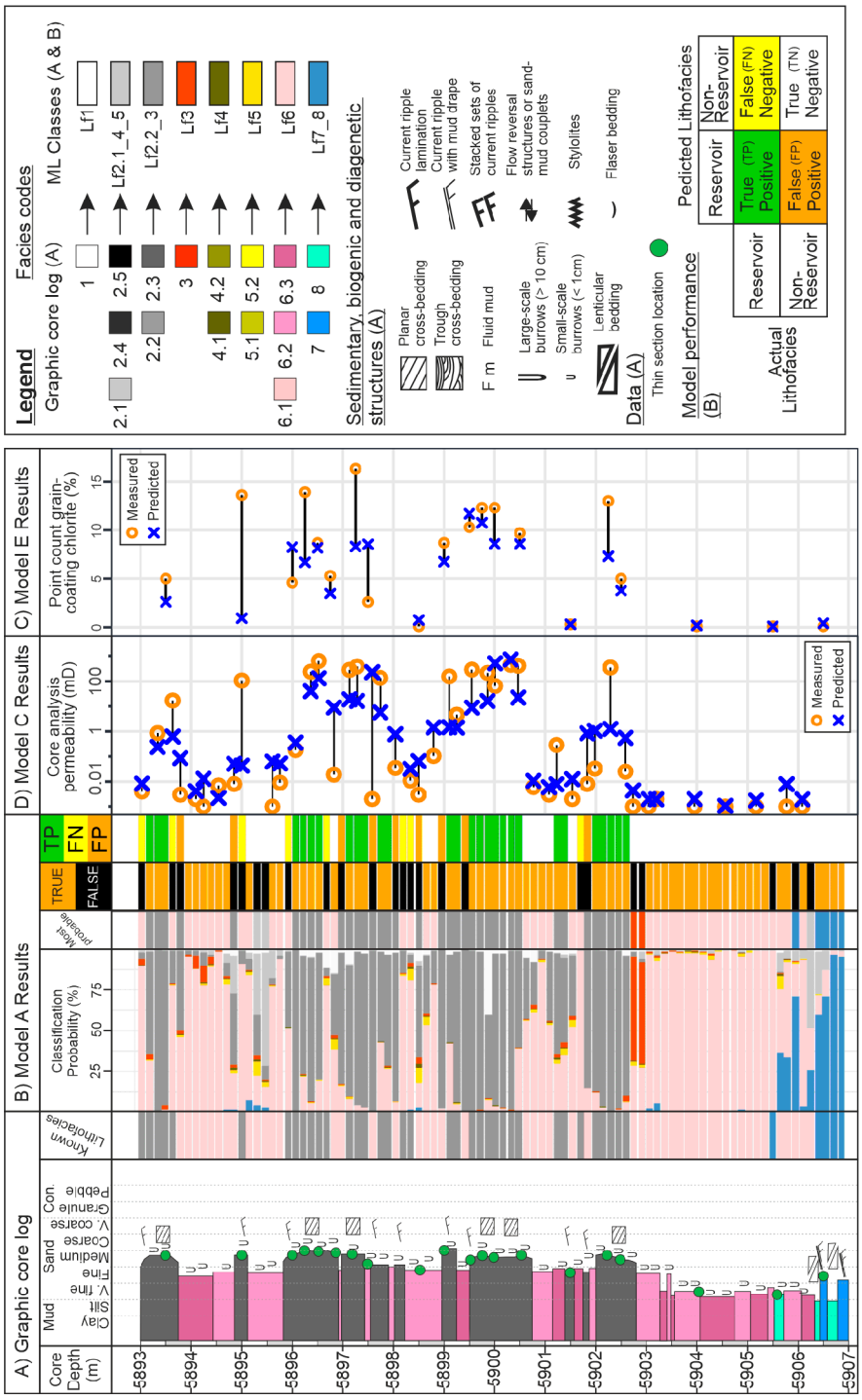

Figure 13. Lithofacies classification logs for reservoir Section 3 between 5893 and 5907 mRKB. Shown is (**A**) a graphic core log indicating grain size, the presence of sedimentary, biogenic, and diagenetic structures, and point-counted thin section samples alongside the assigned lithofacies label for each wireline measurement interval. (**B**) An amalgamation of test results for Model A showing the probability of a given lithofacies label for each interval; the most probable lithofacies label for that wireline interval; a log indicating whether the most probable lithofacies label assigned by the Model A is 'true' or 'false'; an indication of whether a prediction of Lf1 or Lf2.2_3 is a true positive (TP), false negative (FN) or false positive (FP). True negatives are left blank. (**C**) Amalgamated results of Model E point count grain coating chlorite regression prediction. (**D**) Amalgamated results of Model C core analysis permeability regression prediction.

Permeability predictions in Section 1 show minimal errors for most of the section, typically where permeability is low (<0.1 mD). Under-estimations are observed in several high permeability samples between 5979 and 5981.2 mRKB, where an anomalously high permeability interval (compared to the rest of the section) within Lf2.2_3 is not predicted to occur by Model C.

Reservoir Section 2 shows much more variation in permeability compared to section 1 (compare Figures 11D and 12D), as there are three high permeability intervals, two within Lf1, and one within Lf2.2_3 in thick metre-scale beds. The predictions in these high permeability intervals are much more accurate compared to reservoir Section 1; however, errors are observed to occur in the transitional intervals between high and low permeability facies, for example, at 5948.8, 5949.3, and 5952 mRKB, at the boundaries between two contrasting lithofacies.

Reservoir Section 3 exhibits thinly inter-bedded Lf6 and Lf2.2_3, which have contrasting reservoir properties (Figure 13D). Lf6 typically has low permeability because of pore-filling chlorite, whereas Lf2.2_3 has high permeability due to chlorite grain coats. In this section, significant errors occur between predicted and measured values in thin beds, such as in a thin bed of Lf2.2_3 at 5895 mRKB and in a thin bed of Lf6 at 5897.5 mRKB. Generally, the higher measured permeabilities are under-estimated by roughly one order of magnitude, whereas the lower measured permeabilities are over-estimated by Model C by several orders of magnitude.

4.3.2. Model A: Lithofacies Classification

Model A was trained to classify lithofacies using all eight wireline log parameters as predictors (Table 2). The relative importance of each parameter in reducing error for Model A is shown in Figure 14. Deep resistivity (RD) and caliper (CALI) are shown to be the most important predictors of Lithofacies in core 6506/12-N-4H, whereas the two least important are shear (DTS) and compressional (DTCO) sonic logs.

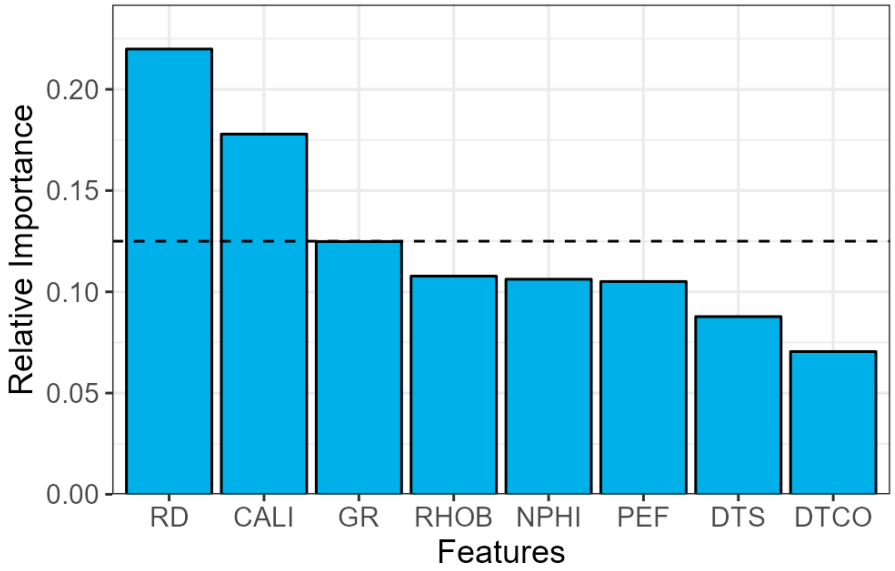

Figure 14. Relative importance of each wireline parameter in reducing error when training Model A to classify lithofacies. The bars above the dashed line represent variables that are above-average contributors to error reduction. (RD = deep resistivity; CALI = caliper; GR = gamma ray; RHOB = bulk density; NPHI = neutron porosity; PEF = photoelectric effect; DTS = shear wave delay; DTCO = compressional wave delay).

The amalgamated results of four folds of training/testing data are presented in the confusion matrix, Figure 15, with associated evaluation metrics for each lithofacies class for

Model A presented in Table 7 The overall accuracy of Model A ranges from 69.4 to 73.9% across all four folds, with a mean overall accuracy of 71.6%.

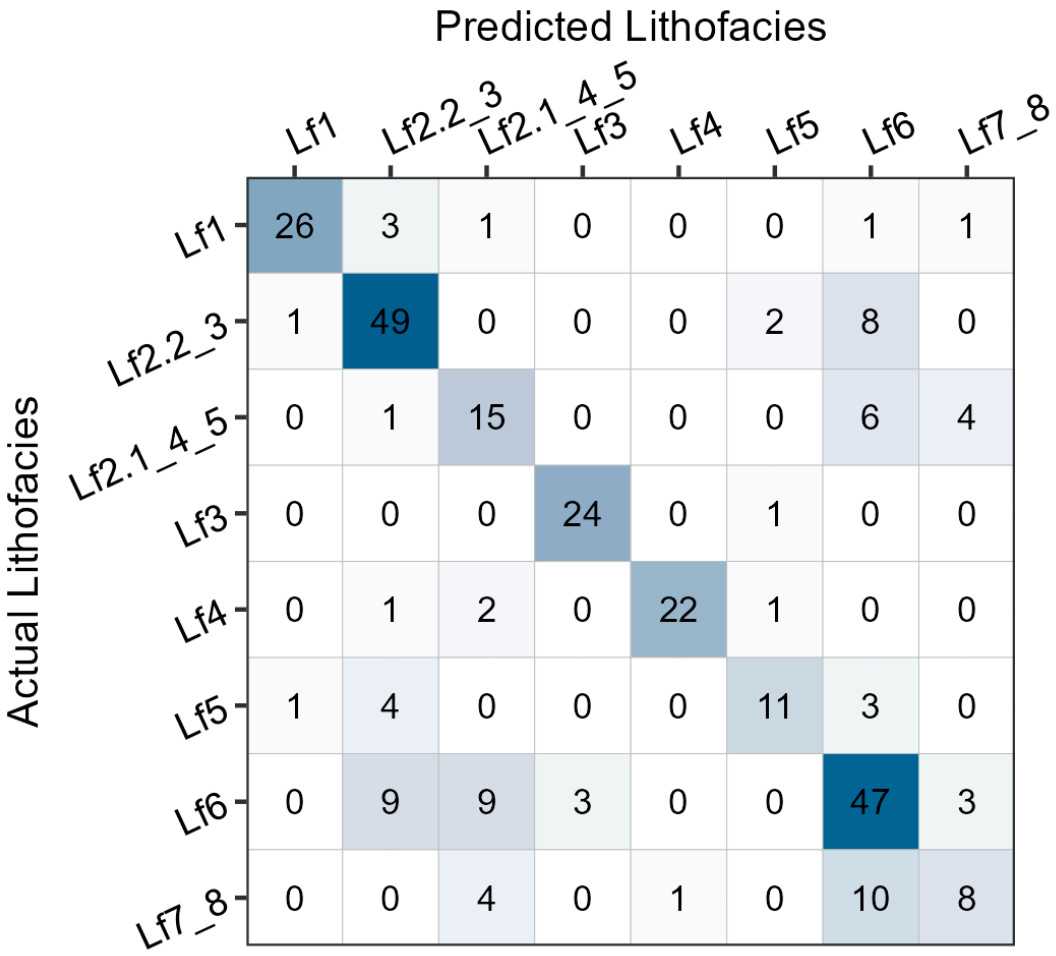

Figure 15. Confusion matrix of predictions of unseen testing data across all four folds of Model A. This matrix consists of rows that represent actual Lithofacies classifications of core intervals, and the columns represent which Lithofacies those intervals are predicted to be. Darker colors indicate a higher number in the cell.

Table 7. Mean evaluation metrics for Model A when classifying testing data for each Lithofacies across 4-folds of training/testing data (one standard deviation in parentheses). Overall accuracy for Model A is 71.6% (1 sd = 1.64%).

Lithofacies	Precision	Recall	F1
Lf1 ($n_{test} \approx 7$)	0.927 (0.074)	0.804 (0.129)	0.853 (0.070)
Lf2.2_3 ($n_{test} \approx 15$)	0.728 (0.061)	0.812 (0.057)	0.767 (0.054)
Lf2.1_4_5 ($n_{test} \approx 5$)	0.492 (0.215)	0.601 (0.244)	0.529 (0.215)
Lf3 ($n_{test} \approx 5$)	0.811 (0.189)	0.977 (0.039)	0.871 (0.124)
Lf4 ($n_{test} \approx 3$)	0.972 (0.048)	0.889 (0.136)	0.922 (0.084)
Lf5 ($n_{test} \approx 4$)	0.775 (0.155)	0.565 (0.157)	0.643 (0.125)
Lf6 ($n_{test} \approx 20$)	0.639 (0.076)	0.670 (0.093)	0.646 (0.044)
Lf7_8 ($n_{test} \approx 13$)	0.600 (0.424)	0.370 (0.377)	0.337 (0.209)

As the purpose of the modelling was to test if reservoir lithofacies Lf1 (cross-stratified sandstone with quartz pebbles) and Lf2.2_3 (cross-stratified sandstone with flasers/bioturbation) could be distinguished from non-reservoir lithofacies, we will focus on the two reservoir lithofacies in the following results and discussion.

The results show that Model A can positively identify Lf1 and Lf2.2_3 intervals with a recall score of 0.804 and 0.812, respectively, indicating a roughly 20% false negative rate for

both classes. It is worth noting that 3 of 32 Lf1 intervals are incorrectly classified as Lf2.2_3 (Figure 15), making up half of the false negatives for Lf1. In this case, the interpretation of reservoir vs. non-reservoir facies would not change significantly when compared to incorrect non-reservoir classifications. False negatives for Lf2.2_3 intervals are mostly in Lf6 (intensely bioturbated heterolithics).

Lf1 has a much higher precision score of 0.927 when compared with Lf2.2_3's score of 0.728, indicating that intervals belonging to other lithofacies may be falsely identified as Lf1 or Lf2.2_3 by Model A at a rate of 7.3% and 27.2% respectively. The confusion matrix shows that false positives for Lf2.2_3 can be attributed mainly to Lf1 (reservoir) and Lf5 and Lf6 (both non-reservoir). Where Lf2.2_3 is predicted instead of a non-reservoir lithofacies, this error could lead to misinterpretation of the well in terms of facies distribution.

Figure 11B illustrates the performance of Model A within reservoir Section 1. With respect to Lf1 and Lf2.2_3 classifications in reservoir Section 1, there are two false negatives (yellow), four false positives (orange), and eight true positives (green), with the remaining 66 intervals true negatives (white). In this section, the false negatives and false positive intervals show significant confusion with adjacent lithofacies classes, as evidenced by the classification probability log, which shows greatest uncertainty (where the probability of classifications is near equal for multiple classes) on the boundary of two lithofacies, particularly between 5982 and 5982 m (Figure 11B). This is surprising as the model is given no information about the relative position of the datapoints, or that they are spatially related at all. In the instances of false negatives at 5979.25 m and false positives at 5980.5 m, the classification probability is very high for the respective outputs, resulting in one bed each of Lf5 and Lf2.2_3 between 5978 and 5981 m whereas a manual classification (i.e., by a trained person) has three beds each of Lf5 and Lf2.2_3 that are interbedded.

In reservoir Section 2, presented in Figure 12, intervals of reservoir facies Lf1 and Lf2.2_3 are more common than in reservoir Section 1, providing a better test for the model predictions. Once again, classification errors occur at the boundaries of lithofacies, such as at 5952 and 5953 m. Where there are contiguous intervals of Lf1 or Lf2.2_3, predictions remain consistently correct for that bed, such as between 5946.8 and 5948.5 m (Figure 12B).

Reservoir Section 3 hosts highly heterolithic interbeds of Lf2.2_3 and Lf6 with Lf7_8 at its base (Figure 13A). In this reservoir section, errors in classification with respect to Lf1 and Lf2.2_3 (false positives and false negatives) are proportionally more common in this section compared to Section 2. Once again, errors are mainly associated with lithofacies boundaries, but also with thin beds, and exhibit confusion only with adjacent lithofacies, apart from at 5902.75 m, where Lf3 is predicted to occur despite not appearing anywhere in this section. Similar to the results for Section 2, in Section 3, Model A appears to simplify the stratigraphy, forming thicker beds with fewer thin interbeds than those interpreted manually.

4.3.3. Model E: Point Counted Grain-Coating Chlorite Regression

Model E was trained to quantify point count grain-coating chlorite (PCGCC) using the eight wireline log parameters as predictors (Table 2). Note that there has been no previous attempt to predict grain-coating chlorite using wireline logs. The importance of these eight parameters for reducing errors in Model E is presented in Figure 16, which reveals that the most important parameter to predict PCGCC is bulk density (RHOB), but neutron porosity (NPHI) and gamma ray (GR) are also shown to be above-average contributors to error reduction. All other parameters have much lower importance values, at <0.091.

Amalgamated predictions of all folds of unseen training data for each reservoir section are presented in log form in Figures 11C, 12C, and 13C, and in Figure 17 as a cross-plot of predicted versus measured values. The performance of each fold of testing data is presented in Table 8 to reveal that folds 1 to 3 have much higher R^2 (greater than 0.68)

compared to fold 4 (R^2 = 0.2608), whereas RMSE and MAE metrics do not have such a significant reduction. This drastic reduction in R^2 may be a result of two outliers, seen as two large underestimates in Figure 17.

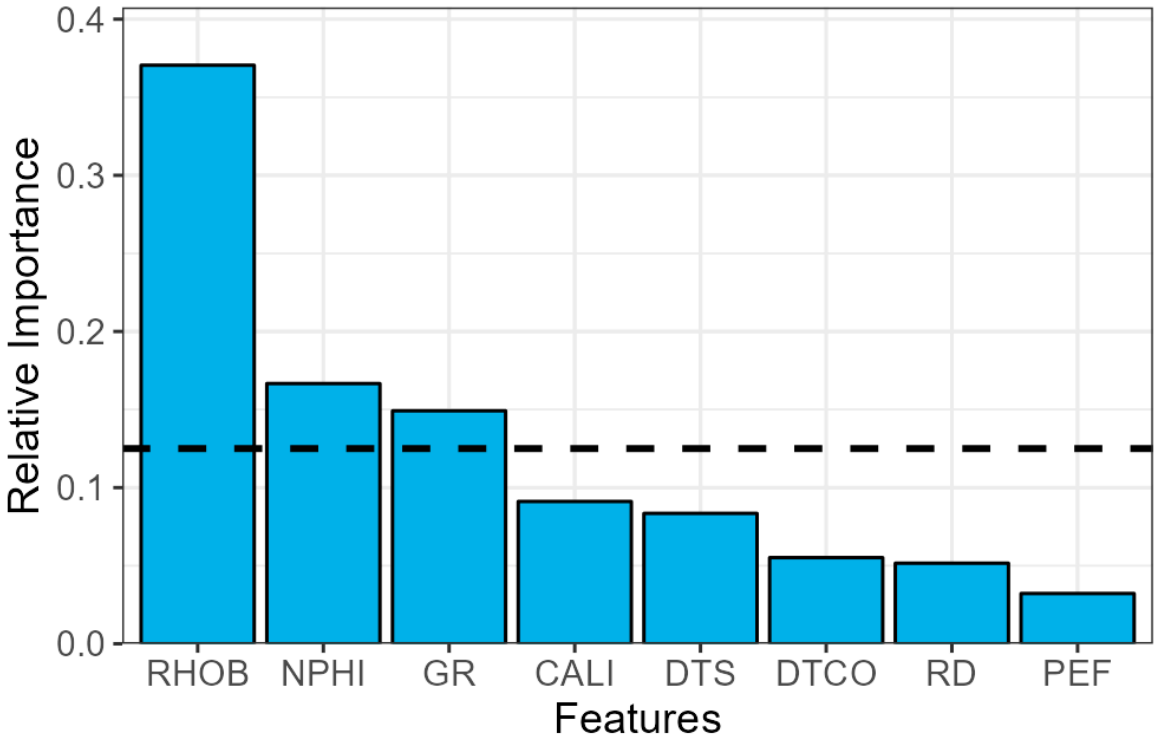

Figure 16. Relative importance of each wireline parameter in reducing error when training Model E to quantify point count grain-coating chlorite. The bars above the dashed line represent variables that are above-average contributors to error reduction. (RHOB = bulk density; NPHI = neutron porosity; GR = gamma ray; CALI = caliper; DTS = shear wave delay; DTCO = compressional wave delay RD = deep resistivity; PEF = photoelectric effect;).

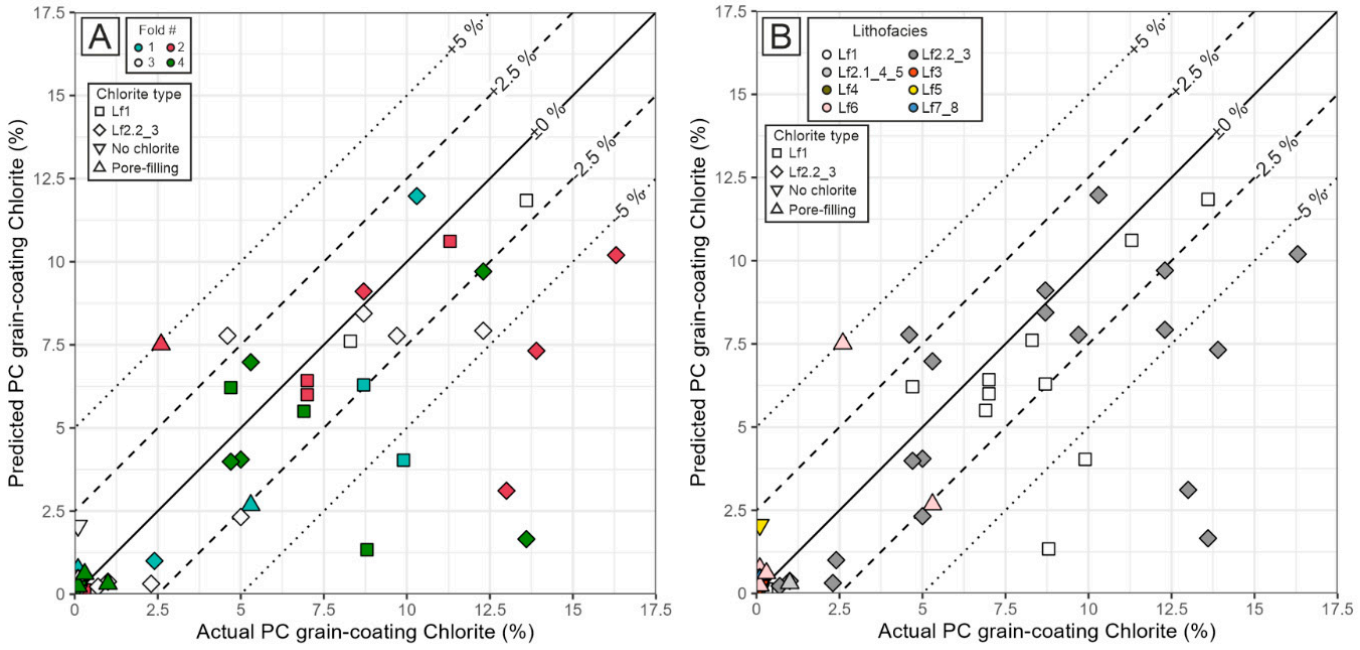

Figure 17. Cross-plots of predicted point-count grain-coating chlorite values vs. measured values, shape-coded for the effects of chlorite in each sample, and colour-coded for: (**A**) data fold, and (**B**) lithofacies.

Table 8. Evaluation metrics for individual folds of Model E testing data. See Table 3 for an explanation of evaluation metrics. These R^2 values can be compared to the prediction of point count grain coating chlorite by linear regression of NPHI, for which $R^2 = 0.537$.

Fold	R^2	RMSE (%)	MAE (%)
1 (n_{test} = 14)	0.8098	1.82	1.00
2 (n_{test} = 14)	0.6842	3.72	2.38
3 (n_{test} = 13)	0.8419	2.01	1.60
4 (n_{test} = 13)	0.2608	4.31	2.33
All (n_{test} = 54)	0.6499	3.11	1.79

Figure 17 shows that under-estimations of predicted PCGC occur more than over-estimations, and the highest value of actual PCGC (16.3%) is predicted as 10.19%, an interval of Lf2.2_3 at 5897.25 m. Under-estimates of 8.8%, predicted as 1.33% (in Lf1) and 13.6%, predicted as 1.68% (in Lf2.2), occur at 5949 m (reservoir Section 2; Figure 12C) and 5895 m (reservoir Section 3; Figure 11C), respectively. A total of 43 predictions lie within ±2.5% of the actual value, including all twenty < 0.1% values, indicating that the model is effective at identifying intervals without porosity-preserving chlorite grain coats. The point with the highest over-estimation (2.6% measured; 7.51% predicted) occurs in a thin (10 cm) bed of Lf6 in reservoir Section 3 at 5897.5 m (Figure 12C).

5. Discussion

5.1. Controls on Wireline Responses; Links to Lithofacies and Chlorite

The effects of chlorite on wireline log responses and its identification using wireline data are topics of discussion in the literature, as they are key to understanding the potential for porosity-preserving grain coats [4,29,61]. Traditionally, the presence of clay minerals is inferred from the gamma ray log due to the presence of radioactive elements such as K, Th, or U. However, in the case of chlorite, an Mg-Fe-rich aluminosilicate ($(Mg,Fe)_{4–6}(Si,Al)_4O_{10}(OH,O)_8$), there are no radioactive elements contained within the crystal structure and so chlorite provides minimal contribution to a gamma ray response [4,27]. Authigenic chlorite platelets are known to retain water within microporosity, resulting in elevated irreducible water saturation, which, if briny, reduces resistivity of the chlorite-bearing interval despite oil emplacement, which would otherwise increase resistivity [29,62,63]. Additionally, the neutron log response of chlorite-bearing rock is theoretically high due to the relatively high number of hydrogen atoms per unit cell [4]. Based on these petrophysical properties of chlorite, Worden, Griffiths, Wooldridge, Utley, Lawan, Muhammed, Simon and Armitage [4] suggested that chlorite-coat-derived enhanced porosity is characterised by low resistivity, high neutron response as a result of the presence of chlorite, and low bulk density and high acoustic delay as a result of the high porosity. Considering the known petrophysical expression of chlorite, it is possible to assess whether the models presented in this study are able to truly exploit the petrophysical expression of chlorite or whether non-unique properties (e.g., high porosity) are more important.

Reservoir lithofacies class Lf1 is shown to have very low bulk density (RHOB) compared to non-reservoir lithofacies and moderately lower when compared to Lf 2.2_3 (Figure 8G). Conversely, Lf1 has very high compressional wave delay (DTCO) compared to non-reservoir lithofacies and moderately higher when compared to Lf2.2_3 (Figure 8H). These differences are highlighted as being statistically significant by ANOVA and post-hoc Tukey Honestly Significant Difference (HSD) test (Table 5), as RHOB and DTCO are shown to be statistically significantly different from all other lithofacies, likely contributing to their high evaluation metric scores for precision, recall, and F1 (all above 0.8; Table 6). The differences between Lf1 and other lithofacies may be a result of the high porosity, which is known to reduce bulk density and increase compressional wave delay time [27,64].

These relationships are also evidenced in the wireline data for this well, as there is a strong negative correlation between core analysis porosity and bulk density (R = −0.856), and a strong positive correlation between core analysis porosity and compressional wave delay (R = 0.744) (Table 5).

Deep resistivity (RD) is shown to be the most important wireline parameter for reducing errors in the model (Figure 9), likely caused by the significant differences between Lf3 which has relatively low resistivity (less than 10 Ωm), Lf4 with high resistivity (more than 20 Ωm), compared to the other lithofacies which have moderately low resistivity, between 10 to 20 Ωm, which are shown graphically in Figure 8J. Statistically, Lf3 and Lf4 have significant differences in deep resistivity values when compared to each other and all other lithofacies, potentially allowing them to be heavily exploited by Model A (Table 5; Figure 8J). Despite these differences for Lf3 and Lf4, the Tukey HSD tests (Table 5) between other lithofacies classes suggest that RD is not a statistically reliable discriminator, as only 5 of 15 other comparisons are significantly different. This may be due to the low chlorite content in Lf4 (Figure 8J,L), and so has not retained elevated irreducible water saturation after oil emplacement, which would lower resistivity [4]. By contrast, other lithofacies have a significant amount of chlorite (Figure 8L), which results in high irreducible water saturation, and lowering resistivity. Neutron porosity is also observed to be higher in reservoir facies, but this is not shown to be a highly important parameter for reducing error (Figure 9).

While the intended utility of Model A is to identify chlorite-coated facies, it is likely only doing this as a proxy through the effects of the grain-coating chlorite rather than directly exploiting the petrophysical response of the grain coats themselves. For example, reservoir lithofacies Lf1, Lf2.2, and Lf2.3 are grain-coated by chlorite, therefore have elevated porosity, resulting in decreased bulk density and increased acoustic delay times. The discrimination of other lithofacies by the model may be attributed to other effects, such as radioactive elements in some clay minerals increasing gamma responses, such as in Lf7_8, which host fluid muds (Figure 8C).

Model E shows that bulk density (RHOB) is the most important parameter in reducing model error, which, similar to previous discussion of links of grain coating chlorite affecting porosity, which affects RHOB rather than a petrophysical response to chlorite (Figure 9). Neutron porosity is the second-most important parameter for reducing error in the Model E which, given the typically high response of chlorite, could indeed be linked to chlorite coat abundance at these intervals as it is shown to have the strongest correlation with chlorite grain coat abundance (R = 0.733) of any of the wireline parameters (Tables 4 and 7).

Here, we suggest that the performance of Model A and E may be influenced by the presence of chlorite directly and indirectly. Deep resistivity and neutron porosity are known to be discriminators of chlorite-bearing rocks, and these responses are possibly being exploited in the modelling as suggested by the high importance of deep resistivity in Model A (Figure 9), and of neutron response in Model E (Figure 14). However, the presence of chlorite as coats may be indirectly used by the model to identify high porosity zones, which coincide with high chlorite grain coat abundance in both Models A and E. The direct effects of chlorite may be exploited by Model A, but only in distinguishing between very high and very low chlorite. However, this chlorite may variably be present in the rock as grain-coating, pore-filling, or grain-replacive types, each of which has different effects on reservoir quality [18,65,66]. Furthermore, the presence of non-reservoir classes, which are discriminated more effectively by other parameters, might dilute the effects of chlorite for lithofacies classification.

5.2. Lithofacies Classification of the Tilje Formation

Sediment texture often acts as a significant control on reservoir quality [67], leading many studies to train models that can identify lithology based predominantly on grain size, with generic class labels such as 'sandstone', 'mudstone', 'siltstone' (e.g., [32,33,59,68,69]). A lithology-based scheme may be sufficient when a reservoir's porosity and permeability are governed by the primary texture of the rock; however, for the many reservoirs where diagenetic processes control reservoir quality, texture-based classes may be inappropriate to infer reservoir quality [15,70,71]. To solve this problem, some authors choose a 'diagenetic facies' label which more accurately reflects the diagenetic controls on reservoir quality compared to lithology, such as in the Yanchang Formation of the Ordos Basin, where the main control on reservoir quality is secondary porosity formed by dissolution of rock fragments and feldspars during mesodiagenesis [39,45]. The lithofacies scheme trained for classification in Model A is defined by grain size characteristics, sedimentary structure, bioturbation, and chlorite presence, linked to sedimentological processes. These properties can then be inferred in intervals where lithofacies predictions could be made in uncored wells, offering an advantage over schemes that require core for detailed facies definition. In addition, the environmental links in the lithofacies scheme could point toward connectivity potential, lateral continuity, or bed morphology. This scheme sits between a strict descriptive nature of lithology and diagenetic controls on reservoir quality, which also influenced merging lithofacies classes prior to model training, such as in the merging of Lf7 and Lf8, which are both non-reservoir due to high pore-filling chlorite and low grain-coating chlorite; distinguishing these two lithofacies does not represent significant value in terms of determining reservoir quality by proxy.

Model A presented in Figures 12–14 has eight distinct classes, which reflect geological variability but not reservoir quality variability. If geological information is of lower value, a user could instead binarize the class predictions into classes such as 'contains chlorite grain coats' and 'does not contain chlorite grain coats', which would also provide information about the presence of chlorite grain coats. In the present study, we chose to keep the eight lithofacies discrete to preserve as much geological information as possible, which may be of use for further modelling and interpretation.

5.3. Sources of Error When Predicting the Presence of Grain-Coating Chlorite Using Machine Learning

The predictions of Lf1 and Lf2.2_3 by Model A appear to perform the worst in the most heterogeneous, and cm-scale interbedded Lf2.2_3 and Lf6 of Section 3 (Figure 13), when compared to the massive, metre-scale bedding of Lf1 and Lf2.2_3 in Section 2 (Figure 12). Also in Section 2, the model predictions fail to recognise the presence of 30 cm-thick interbeds of Lf5 and Lf2.2_3 within larger beds (Figure 12). We suggest that these errors in classification at lithofacies boundaries may be a function of limitations of the acquisition of wireline measurements with respect to sampling volume and resolution, and the tilt of the wellbore with respect to the heterolithic beds, especially a problem in thin-bedded heterolithics. These log resolution and tilted bed issues cause shoulder effects in wireline responses as the log measurements are a combination of the two adjacent lithofacies, which may also explain why classification probabilities for lithofacies boundaries commonly contain high probabilities of classification from adjacent lithofacies. This issue can also be seen to affect quantitative prediction of permeability values by Model C, and grain coating chlorite by Model E, for example, the outliers in reservoir Section 3, where thin beds of contrasting reservoir quality are interbedded. This effect is perhaps most obvious in the bulk density (RHOB) response of facies association 3 (Figure 7A), where contrasting low RHOB values in Lf2.2_3 (approximately 2.3 gcm^{-1}) and high RHOB values in Lf6 (approximately 2.6 gcm^{-1}) are interbedded to produce a fluctuating response (a similar

pattern is observed in shear sonic response, DTS) which may contribute to the model errors observed in Figure 13. In effect, the measurements for a given depth are also capturing responses of adjacent lithofacies as well as that of the 'actual' lithofacies recorded at that interval. The effect of this was also noted as a contributor to difficulty in interpreting the Smørbukk field by Martinius, Ringrose, Brostrom, Elfenbein, Naess and Ringas [24] and the results here are directly affected by this issue.

Similar effects are observed in the regression Model E to predict point count grain coat chlorite (PCGCC) abundance, for example, at 5895 mRKB in reservoir Section 3 (Figure 13), Model E underestimates the amount of PCGCC within the very thin bed of Lf2.3, represented in Figure 17 by the bottom right-most point. This sample lies between thicker beds of Lf6, which likely have lower PCGCC abundances, but the signal of the bed at 5895 mRKB is below the full resolution of the wireline measurement. Similar to the performance of Model A, Model E exhibits confusion at or near lithofacies boundaries between differing PCGCC abundance. An example of this may be seen at the base of the Lf1 package at 5952 mRKB in reservoir Section 2 (Figure 12), where PCGCC is under-estimated, which may be a result of conflicting signals of the PCGCC-poor Lf2.1, which underlies it, represented in Figure 17 by the bottom middle point. The cases where Models A, C, and E have been observed to be accurate or inaccurate are illustrated in Figure 18 which summarises sources of error in the models presented here, specifically in the geological context of this well. One weakness of Model E trained in this study is a low sample size, which may have decreased model performance by not capturing the full extent of petrophysical characteristics of grain-coat chlorite bearing intervals to allow near-perfect prediction. However, due to the practical limitations of sampling core and the time-consuming analyses to obtain permeability and petrographic data, the authors were not able to improve this aspect of the modelling process.

The results presented here represent sub-optimal conditions for the application of machine learning to facies and chlorite coat prediction due to the apparent dip of beds relative to the wellbore and thinly-bedded heterogeneous nature of the deposits, resulting in multiple lithologies being captured in one interval, and the higher likelihood that a bed is below detectable thickness. Log parameters with high penetration depths are most impacted by this effect, such as induction logs and laterologs, but the effect will be lessened in the responses of low penetration depth measurements, such as gamma, density, and sonic logs [27,72]. Here we suggest that the ideal conditions for the application of the method presented are when beds are horizontal relative to the wellbore and where beds are thick enough to allow for full resolution, which, depending on logging conditions, parameters measured, and parameter importance in the desired model (Figures 9, 14, and 16), is between 15 and 90 cm [27,28]. For example, optimal measurements of bulk density, the most important feature in predicting permeability in Model C and chlorite grain coat abundance in Model E (Figure 16), would be when beds are at least 45 cm thick [62]. In contrast, for lithofacies classifications by Model A, when resistivity is the most important feature, thicker beds of at least 76 cm may represent optimal conditions [62]. Although the limitations highlighted to affect model performance in this study have not been accounted for by data curation or transformation (beyond log-transformation), it may be possible to reduce shoulder effects and thin bed effects by deconvolution of petrophysical logs to better discriminate the petrophysical characteristics of facies and grain coating chlorite [27].

Given the limitations and proposed sources of error of the modelling presented, it is suggested that the use of both models (A and C) in tandem can qualitatively suggest the accuracy of the model output. For example, a lithofacies log (synthetic or manual) could highlight interbeds, thin beds, or lithofacies boundaries where predictions of a chlorite grain coat and permeability predictions are likely to be more prone to errors (Figure 16).

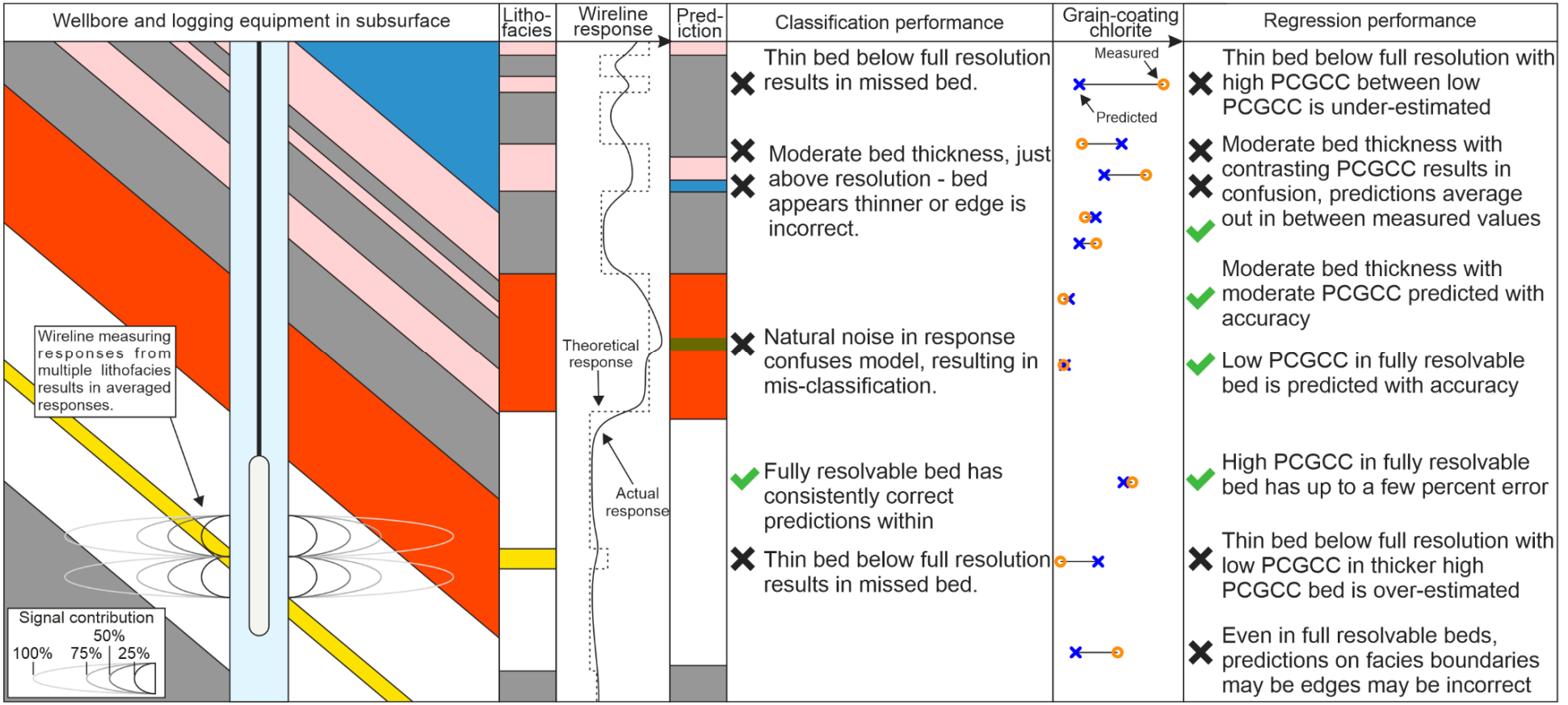

Figure 18. Schematic diagram of subsurface wireline log acquisition with strata (with different beds represented by various colours) inclined relative to the wellbore illustrating how multiple facies may be contributing to the response at a particular depth. A qualitative representation of a theoretical and actual wireline response is shown. Known lithofacies labels are shown compared to machine learning (ML) predictions, and the cause of possible differences is highlighted. Point count grain-coating chlorite (PCGCC) measurements and predictions are also shown, with model performance highlighted.

5.4. Implications for Reservoir Quality Prediction

Multiple authors have highlighted that a lack of understanding of the distribution of cementation in the Tilje Formation has been a significant contributor to difficulties in predicting porosity and permeability in deep fields [24–26,73]. In such fields, reservoir quality is controlled less by sand-to-mud ratio, which may be determined by a 'Vshale' calculation from gamma ray response, and more by variations in cementation as a result of grain-coating chlorite, which cannot be easily distinguished by conventional wireline log characteristics. The workflow presented here to train a machine learning model to identify lithofacies in a chlorite-cemented heterolithic marginal marine sandstone such as the Tilje Formation represents a step toward developing tools which can (1) increase our understanding of the distribution of facies-controlled cementation at the same resolution as wireline data and (2) potentially facilitate stochastic modelling to build a three-dimensional reservoir-scale facies model by using lithofacies predictions (and probabilities thereof) made by Model A [25,74,75]. Incorporating the machine learning workflow presented here into field-scale reservoir characterisation involving multiple wells could reduce uncertainty by providing a geological interpretation of a wireline log without the need for collecting core, thereby also reducing costs.

Being able to predict the distribution of chlorite-bearing facies using wireline log data represents value in comparison to purely core-based determination, which requires very expensive acquisition of core and then petrographic studies. The core-calibrated predictive model created here can be applied to uncored intervals from the same well or to a different well, increasing the value of the acquired core and wireline data. However, a user of field/formation-specific models should be careful to ensure that the regional and stratigraphic context of the model's basis is well-understood, i.e., the user should develop such a model for wells, intervals, or fields which share sedimentary environments and reservoir quality controls. For example, the models trained here in the deep Tilje Formation of the Smørbukk field are not suitable for application in time-equivalent intervals in shallower fields such as Heidrun, where grain coats are absent and instead calcite cementation controls reservoir quality (Figure 1) [24]. Similarly, the model may be unsuitable to predict chlorite-coated intervals in different formations, such as the overlying Tofte Formation, which, despite hosting chlorite grain coats, was deposited in a different sedimentary environment and so could contain environment-specific facies that are not accounted for by a Tilje-calibrated model (Figure 2) [21]. Given training data from multiple cored wells in the Tilje Formation of the Smørbukk field, it would be possible to train a generalised model capable of reliable field-wide formation-specific prediction of lithofacies distribution and grain coat abundance [31,34]. Including data from multiple wells would increase sample size for each lithofacies, and capture reservoir-scale heterogeneities within the formation in contrast to the smaller core-scale heterogeneities captured in the models of the study; this is a key issue to consider in heterolithic tide-influenced and tide-dominated successions whose multi-scale heterogeneity is well-documented [24,76–78].

When training a model using multiple wells, other non-geological factors must be considered that affect the quality of well log responses, thereby affecting model performance and prediction. For example, log data obtained can be affected by the type of drilling fluid, particularly affecting resistivity (conductive vs. non-conductive mud) and caliper logs (due to mud cake build-up) [27]. Age and equipment manufacturer also impact data acquisition, as not all measurement equipment records the full suite of logs that are utilised in this study. In addition, as observed in well 6506/12-N-4H, well deviation affects measurements and produces shoulder effects (Figures 5–7), the consequences of which would be different in vertical or horizontal wells. Considering these wide-ranging effects of data acquisition

limitations, it may be necessary to process data prior to model training when handling data from multiple wells with different equipment, age, and logging environments.

6. Conclusions

This study focused on the heterolithic tide-dominated Tilje Formation in three reservoir sections of well 6506/12-N-4H of the Smørbukk field of the Norwegian North Sea, where porosity is preserved (up to 26%) at great depths (>4 km) due to the presence of grain-coating chlorite, which has inhibited quartz cementation. Due to the multi-scale heterogeneous nature of the formation, predicting the distribution of chlorite grain coats using traditional approaches is challenging. Here we test the ability of machine learning models (using an Extreme Gradient Boost-based workflow) to predict lithofacies (as a proxy for grain-coat presence) and grain-coating chlorite abundance using eight measured wireline log parameters as predictors. We quantify the performance of the two models, and, by exploring the statistical and geological relationships between predictors and labels, we discuss how geological factors affect model performance.

Statistical differences between eight wireline log responses as a function of lithofacies have been described and identified, where these differences are statistically significant. Differences in wireline log responses between lithofacies are likely linked to differences in mud content, chlorite content, and cementation, which are controlled by primary depositional and secondary diagenetic factors.

The statistical relationships between wireline responses, lithofacies, and chlorite coat abundance provide a basis to create a machine learning classification model to predict lithofacies and grain-coating chlorite abundance using wireline responses as predictors.

Model C is a regression model trained to quantitatively predict horizontal permeability based on eight wireline parameters. Across four folds of training/testing data, the correlation coefficient (R^2) between predictions and measurements of unseen log-permeability data is 0.6928, root mean square error of 1.09, and mean absolute error of 0.782.

Model A is a classification model trained to predict lithofacies in three reservoir sections. Across four folds of training/testing data, the mean overall accuracy of the model is 76.1%. Reservoir lithofacies can be distinguished from non-reservoir lithofacies with approximately 80% accuracy.

Model E is a regression model trained to quantitatively predict the amount of grain-coating chlorite in an interval, calibrated using petrographic point counting data. Grain-coating chlorite has never previously been predicted from wireline log data. In the training data set of 54, grain coating chlorite abundance varies between 0 and 16.1%. The model is able to predict the quantity with an R^2 value of 0.6499, root mean square error of 3.11% and mean absolute error of 1.79%.

Thin beds at or below the resolution of wireline data acquisition, where lithofacies are interbedded with bed thicknesses of less than 30 cm, may be missed by the classification prediction, resulting in poor model performance compared to the core.

Where beds are thick (>30 cm), model predictions are good, but there may be errors in classification or quantification at boundaries.

The deviated nature of the well that we have worked on also results in model confusion, as, during acquisition, multiple lithofacies may contribute to the log measurement, causing further confusion in the model predictions.

Author Contributions: Conceptualisation, T.E.N. and R.H.W.; methodology, T.E.N. and J.E.H.; formal analysis, T.E.N. and J.E.H.; writing—original draft preparation, T.E.N.; writing—review and editing, R.H.W., J.E.H., J.G., C.B. and A.W.M.; visualisation, T.E.N., J.E.H. and J.G.; supervision, R.H.W.; funding acquisition, R.H.W. All authors have read and agreed to the published version of the manuscript.

Funding: The project was supported by BP, Equinor, and DNO.

Data Availability Statement: The modelling codes are available in the open access repository at: zenodo,org, file 15236033. Data presented in this study are available on request from the corresponding author.

Acknowledgments: This work was completed as part of the Chlorite Consortium at the University of Liverpool.

Conflicts of Interest: Author Christian Brostrøm and Allard W Martinius were employed by the company Equinor ASA. The remaining authors declare that the research was conducted in the absence of any commercial or financial relationships that could be construed as a potential conflict of interest.

References

1. Dowey, P.J.; Hodgson, D.M.; Worden, R.H. Pre-Requisites, Processes, and Prediction of Chlorite Grain Coatings in Petroleum Reservoirs: A Review of Subsurface Examples. *Mar. Pet. Geol.* **2012**, *32*, 63–75. [CrossRef]
2. Charlaftis, D.; Jones, S.J.; Dobson, K.J.; Crouch, J.; Acikalin, S. Experimental Study of Chlorite Authigenesis and Influence on Porosity Maintenance in Sandstones. *J. Sediment. Res.* **2021**, *91*, 197–212. [CrossRef]
3. Aagaard, P.; Jahren, J.S.; Harstad, A.O.; Nilsen, O.; Ramm, M. Formation of Grain-Coating Chlorite in Sandstones. Laboratory Synthesized Vs. Natural Occurrences. *Clay Miner.* **2000**, *35*, 261–269. [CrossRef]
4. Worden, R.H.; Griffiths, J.; Wooldridge, L.J.; Utley, J.E.P.; Lawan, A.Y.; Muhammed, D.D.; Simon, N.; Armitage, P.J. Chlorite in Sandstones. *Earth Sci.-Rev.* **2020**, *204*, 103105.
5. Gould, K.; Pe-Piper, G.; Piper, D.J.W. Relationship of Diagenetic Chlorite Rims to Depositional Facies in Lower Cretaceous Reservoir Sandstones of the Scotian Basin. *Sedimentology* **2010**, *57*, 587–610. [CrossRef]
6. Ajdukiewicz, J.M.; Larese, R.E. How Clay Grain Coats Inhibit Quartz Cement and Preserve Porosity in Deeply Buried Sandstones: Observations and Experiments. *Am. Assoc. Pet. Geol. Bull.* **2012**, *96*, 2091–2119.
7. Taylor, T.R.; Giles, M.R.; Hathon, L.A.; Diggs, T.N.; Braunsdorf, N.R.; Birbiglia, G.V.; Kittridge, M.G.; Macaulay, C.I.; Espejo, I.S. Sandstone Diagenesis and Reservoir Quality Prediction: Models, Myths, and Reality. *Am. Assoc. Pet. Geol. Bull.* **2010**, *94*, 1093–1132.
8. Walderhaug, O. Kinetic Modeling of Quartz Cementation and Porosity Loss in Deeply Buried Sandstone Reservoirs. *Am. Assoc. Pet. Geol. Bull.* **1996**, *80*, 731–745.
9. Wooldridge, L.J.; Worden, R.H.; Griffiths, J.; Utley, J.E. Clay-Coated Sand Grains in Petroleum Reservoirs: Understanding Their Distribution Via a Modern Analogue. *J. Sediment. Res.* **2017**, *87*, 338–352. [CrossRef]
10. Hillier, S. Pore-Lining Chlorite in Siliciclastic Reservoir Sandstones-Electron Microprobe, Sem and Xrd Data, Implications for Their Origin. *Clay Miner.* **1994**, *29*, 665–679.
11. Ryan, P.C.; Reynolds, R.C. The Origin and Diagenesis of Grain-Coating Serpentine-Chlorite in Tuscaloosa Formation Sandstone, Us Gulf Coast. *Am. Mineral.* **1996**, *81*, 213–225. [CrossRef]
12. Ajdukiewicz, J.M.; Nicholson, P.H.; Esch, W.L. Prediction of Deep Reservoir Quality Using Early Diagenetic Process Models in the Jurassic Norphlet Formation, Gulf of Mexico. *Am. Assoc. Pet. Geol. Bull.* **2010**, *94*, 1189–1227. [CrossRef]
13. Li, K.; Xi, K.; Cao, Y.; Niu, X.; Wu, S.; Feng, S.; You, Y. Chlorite Authigenesis and Its Impact on Reservoir Quality in Tight Sandstone Reservoirs of the Triassic Yanchang Formation, Southwestern Ordos Basin, China. *J. Pet. Sci. Eng.* **2021**, *205*, 108843. [CrossRef]
14. Zhu, S.F.; Wang, X.X.; Qin, Y.; Jia, Y.; Zhu, X.M.; Zhang, J.T.; Hu, Y.Q. Occurrence and Origin of Pore-Lining Chlorite and Its Effectiveness on Preserving Porosity in Sandstone of the Middle Yanchang Formation in the Southwest Ordos Basin. *Appl. Clay Sci.* **2017**, *148*, 25–38. [CrossRef]
15. Bello, A.M.; Jones, S.; Gluyas, J.; Acikalin, S.; Cartigny, M. Role Played by Clay Content in Controlling Reservoir Quality of Submarine Fan System, Forties Sandstone Member, Central Graben, North Sea. *Mar. Pet. Geol.* **2021**, *128*, 105058. [CrossRef]
16. Aro, O.E.; Jones, S.J.; Meadows, N.S.; Gluyas, J.; Charlaftis, D. The Importance of Facies, Grain Size and Clay Content in Controlling Fluvial Reservoir Quality–an Example from the Triassic Skagerrak Formation, Central North Sea, Uk. *Pet. Geosci.* **2023**, *29*, 2022–2043. [CrossRef]
17. Stricker, S.; Jones, S.J. Enhanced Porosity Preservation by Pore Fluid Overpressure and Chlorite Grain Coatings in the Triassic Skagerrak, Central Graben, North Sea, UK. In *Reservoir Quality of Clastic and Carbonate Rocks: Analysis, Modelling and Prediction*; Armitage, P.J., Butcher, A.R., Churchill, J.M., Csoma, A.E., Hollis, C., Lander, R.H., Omma, J.E., Worden, R.H., Eds.; Geological Society of London: London, UK, 2018; pp. 321–341.
18. Griffiths, J.; Worden, R.H.; Utley, J.E.; Brostrøm, C.; Martinius, A.W.; Lawan, A.Y.; Al-Hajri, A.I. Origin and Distribution of Grain-Coating and Pore-Filling Chlorite in Deltaic Sandstones for Reservoir Quality Assessment. *Mar. Pet. Geol.* **2021**, *134*, 105326. [CrossRef]

19. Ramm, M.; Bjørlykke, K. Porosity Depth Trends in Norwegian Reservoirs-Assessing the Quantitative Effects of Varying Pore-Pressure, Temperature History and Mineralogy, Norwegian Shelf Data. *Clay Miner.* **1994**, *29*, 475–490. [CrossRef]
20. Ehrenberg, S.N. Preservation of Anomalously High-Porosity in Deeply Buried Sandstones by Grain Coating Chlorite-Examples from the Norwegian Continental Shelf. *Am. Assoc. Pet. Geol. Bull.* **1993**, *77*, 1260–1286.
21. Bloch, S.; Lander, R.H.; Bonnell, L. Anomalously High Porosity and Permeability in Deeply Buried Sandstone Reservoirs: Origin and Predictability. *Am. Assoc. Pet. Geol. Bull.* **2002**, *86*, 301–328.
22. Jahren, J.; Olsen, E.; Bjørlykke, K. Chlorite Coatings in Deeply Buried Sandstones-Examples from the Norwegian Continental Shelf. In *Water-Rock Interaction*; Arehart, G.B., Hulston, J.R., Eds.; Springer: Dordrecht, The Netherlands, 1998.
23. Martinius, A.W.; Kaas, I.; Naess, A.; Helgesen, G.; Kjaerefjord, J.M. Sedimentology of the Heterolithic and Tide-Dominated Tilje Formation. In *Proceedings of the Norwegian Petroleum Society Conference Volume 10: Sedimentary Environments Offshore Norway—Palaeozoic to Recent*; Martinsen, O.J., Dreyer, T., Eds.; Norwegian Petroleum Society: Oslo, Norway, 2001; pp. 103–144.
24. Martinius, A.W.; Ringrose, P.S.; Brostrom, C.; Elfenbein, C.; Naess, A.; Ringas, J.E. Reservoir Challenges of Heterolithic Tidal Sandstone Reservoirs in the Halten Terrace, Mid-Norway. *Pet. Geosci.* **2005**, *11*, 3–16. [CrossRef]
25. Nordahl, K.; Ringrose, P.S.; Wen, R. Petrophysical Characterization of a Heterolithic Tidal Reservoir Interval Using a Process-Based Modelling Tool. *Pet. Geosci.* **2005**, *11*, 17–28. [CrossRef]
26. Ringrose, P.; Nordahl, K.; Wen, R. Vertical Permeability Estimation in Heterolithic Tidal Deltaic Sandstones. *Pet. Geosci.* **2005**, *11*, 29–36. [CrossRef]
27. Rider, M.; Kennedy, M.J. *The Geological Interpretation of Well Logs*; Rider-French Consulting: Cambridge, UK, 2011.
28. Worthington, P.F. Effective Integration of Core and Log Data. *Mar. Pet. Geol.* **1994**, *11*, 457–466. [CrossRef]
29. Durand, C.; Brosse, E.; Cerepi, A. Effect of Pore-Lining Chlorite on Petrophysical Properties of Low-Resistivity Sandstone Reservoirs. *SPE Reserv. Eval. Eng.* **2001**, *4*, 231–239. [CrossRef]
30. Sarker, I.H. Machine Learning: Algorithms, Real-World Applications and Research Directions. *SN Comput. Sci.* **2021**, *2*, 160. [CrossRef] [PubMed]
31. Yasin, Q.; Sohail, G.M.; Khalid, P.; Baklouti, S.; Du, Q. Application of Machine Learning Tool to Predict the Porosity of Clastic Depositional System, Indus Basin, Pakistan. *J. Pet. Sci. Eng.* **2021**, *197*, 107975. [CrossRef]
32. Saporetti, C.M.; da Fonseca, L.G.; Pereira, E. A Lithology Identification Approach Based on Machine Learning with Evolutionary Parameter Tuning. *IEEE Geosci. Remote Sens. Lett.* **2019**, *16*, 1819–1823. [CrossRef]
33. Liu, M.; Hu, S.; Zhang, J.; Zou, Y. Methods for Identifying Complex Lithologies from Log Data Based on Machine Learning. *Unconv. Resour.* **2023**, *3*, 20–29. [CrossRef]
34. Hansen, H.N.; Haile, B.G.; Müller, R.; Jahren, J. New Direction for Regional Reservoir Quality Prediction Using Machine Learning-Example from the Stø Formation, Sw Barents Sea, Norway. *J. Pet. Sci. Eng.* **2023**, *220*, 111149. [CrossRef]
35. Sokolova, M.; Lapalme, G. A Systematic Analysis of Performance Measures for Classification Tasks. *Inf. Process. Manag.* **2009**, *45*, 427–437. [CrossRef]
36. Murphy, K.P. *Probabilistic Machine Learning: An Introduction*; MIT Press: Cambridge, MA, USA, 2022.
37. Nichols, T.; Worden, R.; Houghton, J.; Duller, R.; Griffiths, J.; Utley, J. Sediment Texture and Geochemistry as Predictors of Sub-Depositional Environment in a Modern Estuary Using Machine Learning: A Framework for Investigating Clay-Coated Sand Grains. *Sediment. Geol.* **2023**, *458*, 106530. [CrossRef]
38. Houghton, J.E.; Nichols, T.E.; Griffiths, J.; Simon, N.; Utley, J.E.P.; Duller, R.A.; Worden, R.H. Automated Classification of Estuarine Sub-Depositional Environment Using Sediment Texture. *J. Geophys. Res. Earth Surf.* **2023**, *128*, e2022JF006891. [CrossRef]
39. Cui, Y.F.; Wang, G.W.; Jones, S.J.; Zhou, Z.L.; Ran, Y.; Lai, J.; Li, R.J.; Deng, L. Prediction of Diagenetic Facies Using Well Logs-a Case Study from the Upper Triassic Yanchang Formation, Ordos Basin, China. *Mar. Pet. Geol.* **2017**, *81*, 50–65. [CrossRef]
40. Kamali, M.Z.; Davoodi, S.; Ghorbani, H.; Wood, D.A.; Mohamadian, N.; Lajmorak, S.; Rukavishnikov, V.S.; Taherizade, F.; Band, S.S. Permeability Prediction of Heterogeneous Carbonate Gas Condensate Reservoirs Applying Group Method of Data Handling. *Mar. Pet. Geol.* **2022**, *139*, 105597. [CrossRef]
41. Anifowose, F.; Abdulraheem, A.; Al-Shuhail, A. A Parametric Study of Machine Learning Techniques in Petroleum Reservoir Permeability Prediction by Integrating Seismic Attributes and Wireline Data. *J. Pet. Sci. Eng.* **2019**, *176*, 762–774. [CrossRef]
42. Akande, K.O.; Owolabi, T.O.; Olatunji, S.O.; AbdulRaheem, A. A Hybrid Particle Swarm Optimization and Support Vector Regression Model for Modelling Permeability Prediction of Hydrocarbon Reservoir. *J. Pet. Sci. Eng.* **2017**, *150*, 43–53. [CrossRef]
43. Abbas, M.A.; Al-Mudhafar, W.J.; Wood, D.A. Improving Permeability Prediction in Carbonate Reservoirs through Gradient Boosting Hyperparameter Tuning. *Earth Sci. Inform.* **2023**, *16*, 3417–3432. [CrossRef]
44. Chen, Z.; Gao, J.; Pang, H.; Huo, Z.; Sun, N.; Lv, Y.; Wang, Y.; Wu, B. A Prediction Method for Favorable Hydrocarbon Accumulation Areas in Carbonate Oil Reservoirs Based on Machine Learning and Driven by Formation Water Chemical Characteristic Data. *Carbonates Evaporites* **2024**, *39*, 97. [CrossRef]
45. Deng, T.; Xu, C.; Lang, X.; Doveton, J. Diagenetic Facies Classification in the Arbuckle Formation Using Deep Neural Networks. *Math. Geosci.* **2021**, *53*, 1491–1512. [CrossRef]

46. Ichaso, A.A.; Dalrymple, R.W. Tide-and Wave-Generated Fluid Mud Deposits in the Tilje Formation (Jurassic), Offshore Norway. *Geology* **2009**, *37*, 539–542. [CrossRef]
47. Ichaso, A.A.; Dalrymple, R.W.; Martinius, A.W. Basin Analysis and Sequence Stratigraphy of the Synrift Tilje Formation (Lower Jurassic), Halten Terrace Giant Oil and Gas Fields, Offshore Mid-Norway. *Am. Assoc. Pet. Geol. Bull.* **2016**, *100*, 1329–1375. [CrossRef]
48. Marsh, N.; Imber, J.; Holdsworth, R.E.; Brockbank, P.; Ringrose, P. The Structural Evolution of the Halten Terrace, Offshore Mid-Norway: Extensional Fault Growth and Strain Localisation in a Multi-Layer Brittle-Ductile System. *Basin Res.* **2010**, *22*, 195–214. [CrossRef]
49. Ichaso, A.A.; Dalrymple, R.W. Eustatic, Tectonic and Climatic Controls on an Early Syn-Rift Mixed-Energy Delta, Tilje Formation (Early Jurassic, Smørbukk Field, Offshore Mid-Norway). In *From Depositional Systems to Sedimentary Successions on the Norwegian Continental Margin*; International Association of Sedimentologists; Special Publication; Blackwell Publishing: Oxford, UK, 2014; Volume 46, pp. 339–388.
50. Taylor, A.M.; Goldring, R. Description and Analysis of Bioturbation and Ichnofabrics. *J. Geol. Soc.* **1993**, *150*, 141–148. [CrossRef]
51. Ainsworth, R.B.; Vakarelov, B.K.; Nanson, R.A. Dynamic Spatial and Temporal Prediction of Changes in Depositional Processes on Clastic Shorelines: Toward Improved Subsurface Uncertainty Reduction and Management. *Am. Assoc. Pet. Geol. Bull.* **2011**, *95*, 267–297. [CrossRef]
52. R Core Team. *R: A Language and Environment for Statistical Computing*; R Foundation for Statistical Computing: Vienna, Austria, 2020.
53. Chen, T.; Guestrin, C. Xgboost. In Proceedings of the 22nd ACM SIGKDD International Conference on Knowledge Discovery and Data Mining, California, CA, USA; Association for Computing Machinery: New York, NY, USA, 2016; pp. 785–794.
54. Chen, T.; He, T.; Benesty, M.; Khotilovich, V.; Tang, Y.; Cho, H.; Chen, K.; Mitchell, R.; Cano, I.; Zhou, T.; et al. Xgboost: Extreme Gradient Boosting. R package version 1.6.0.1, 2022. Available online: https://github.com/dmlc/xgboost (accessed on 1 January 2023).
55. Kuhn, M.; Wickham, H. Tidymodels: A Collection of Packages for Modeling and Machine Learning Using Tidyverse Principles, 2020. Available online: https://www.tidymodels.org/ (accessed on 1 January 2023).
56. Zheng, D.; Hou, M.; Chen, A.; Zhong, H.; Qi, Z.; Ren, Q.; You, J.; Wang, H.; Ma, C. Application of Machine Learning in the Identification of Fluvial-Lacustrine Lithofacies from Well Logs: A Case Study from Sichuan Basin, China. *J. Pet. Sci. Eng.* **2022**, *215*, 110610. [CrossRef]
57. Zhong, R.; Johnson, R., Jr.; Chen, Z. Generating Pseudo Density Log from Drilling and Logging-While-Drilling Data Using Extreme Gradient Boosting (Xgboost). *Int. J. Coal Geol.* **2020**, *220*, 103416. [CrossRef]
58. Tharwat, A. Classification Assessment Methods. *Appl. Comput. Inform.* **2020**, *17*, 168–192. [CrossRef]
59. Sun, Z.; Jiang, B.; Li, X.; Li, J.; Xiao, K. A Data-Driven Approach for Lithology Identification Based on Parameter-Optimized Ensemble Learning. *Energies* **2020**, *13*, 3903. [CrossRef]
60. Chicco, D.; Warrens, M.J.; Jurman, G. The Coefficient of Determination R-Squared Is More Informative Than Smape, Mae, Mape, Mse and Rmse in Regression Analysis Evaluation. *PeerJ Comput. Sci.* **2021**, *7*, e623. [CrossRef]
61. Tudge, J.; Lovell, M.; Davies, S.; Millar, M. A Novel Integrated Approach to Estimating Hydrocarbon Saturation in the Presence of Pore-Lining Chlorites. *Pet. Geosci.* **2014**, *20*, 201–209. [CrossRef]
62. Worthington, P.F. Recognition and Evaluation of Low-Resistivity Pay. *Pet. Geosci.* **2000**, *6*, 77–92. [CrossRef]
63. Pratama, E.; Ismail, M.S.; Ridha, S. An Integrated Workflow to Characterize and Evaluate Low Resistivity Pay and Its Phenomenon in a Sandstone Reservoir. *J. Geophys. Eng.* **2017**, *14*, 513–519. [CrossRef]
64. Hook, J.R. An Introduction to Porosity. *Petrophysics-SPWLA J. Form. Eval. Reserv. Descr.* **2003**, *44*, SPWLA-2003-v44n3a4.
65. Bahlis, A.B.; De Ros, L.F. Origin and Impact of Authigenic Chlorite in the Upper Cretaceous Sandstone Reservoirs of the Santos Basin, Eastern Brazil. *Pet. Geosci.* **2013**, *19*, 185–199. [CrossRef]
66. Billault, V.; Beaufort, D.; Baronnet, A.; Lacharpagne, J.C. A Nanopetrographic and Textural Study of Grain-Coating Chlorites in Sandstone Reservoirs. *Clay Miner.* **2003**, *38*, 315–328. [CrossRef]
67. Beard, D.C.; Weyl, P.K. Influence of Texture on Porosity and Permeability of Unconsolidated Sand. *Am. Assoc. Pet. Geol. Bull.* **1973**, *57*, 349–369.
68. Mohamed, I.M.; Mohamed, S.; Mazher, I.; Chester, P. Formation Lithology Classification: Insights into Machine Learning Methods. In Proceedings of the SPE Annual Technical Conference and Exhibition 2019, Calgary, AB, Canada, 30 September–2 October 2019.
69. Xie, Y.; Zhu, C.; Zhou, W.; Li, Z.; Liu, X.; Tu, M. Evaluation of Machine Learning Methods for Formation Lithology Identification: A Comparison of Tuning Processes and Model Performances. *J. Pet. Sci. Eng.* **2018**, *160*, 182–193. [CrossRef]
70. Bloch, S.; Helmold, K.P. Approaches to Predicting Reservoir Quality in Sandstones. *Am. Assoc. Pet. Geol. Bull.* **1995**, *79*, 97–115.
71. Azzam, F.; Blaise, T.; Patrier, P.; Elmola, A.A.; Beaufort, D.; Portier, E.; Brigaud, B.; Barbarand, J.; Clerc, S. Diagenesis and Reservoir Quality Evolution of the Lower Cretaceous Turbidite Sandstones of the Agat Formation (Norwegian North Sea): Impact of Clay Grain Coating and Carbonate Cement. *Mar. Pet. Geol.* **2022**, *142*, 105768. [CrossRef]
72. Mondol, N.H. *Well Logging: Principles, Applications and Uncertainties*; Springer: Berlin/Heidelberg, Germany, 2015; pp. 385–425.

73. Klefstad, L.; Kvarsvik, S.; Ringås, J.E.; Stene, J.J.; Sundsby, O. Characterization of Deeply Buried Heterolithic Tidal Reservoirs in the Smørbukk Field Using Inverted Post-Stack Seismic Acoustic Impedance. *Pet. Geosci.* **2005**, *11*, 47–56. [CrossRef]
74. Olsen, T.; Rosvoll, K.; Kjærefjord, J.; Arnesen, D.; Sandsdalen, C.; Jørgenvåg, S.; Langlais, V.; Svela, K. Integrated Reservoir Characterization and Uncertainty Analysis, Heidrun Field, Norway. In *Petroleum Geology of Northwest Europe: Proceedings of the 5th Conference*; Fleet, A.J., Boldy, S.A.R., Eds.; Geological Society of London: London, UK, 1999; pp. 1209–1220.
75. Brandsæter, I.; McIlroy, D.; Lia, O.; Ringrose, P.; Næss, A. Reservoir Modelling and Simulation of Lajas Formation Outcrops (Argentina) to Constrain Tidal Reservoirs of the Halten Terrace (Norway). *Pet. Geosci.* **2005**, *11*, 37–46. [CrossRef]
76. Churchill, J.M.; Poole, M.T.; Skarpeid, S.S.; Wakefield, M.I. Stratigraphic Architecture of the Knarr Field, Norwegian North Sea: Sedimentology and Biostratigraphy of an Evolving Tide- to Wave-Dominated Shoreline System. In *Sedimentology of Paralic Reservoirs: Recent Advances*; Hampson, G.J., Reynolds, A.D., Kostic, B., Wells, M.R., Eds.; Geological Society of London: London, UK, 2017; pp. 35–58.
77. Gupta, R.; Johnson, H.D. Characterization of Heterolithic Deposits Using Electrofacies Analysis in the Tide-Dominated Lower Jurassic Cook Formation (Gullfaks Field, Offshore Norway). *Pet. Geosci.* **2001**, *7*, 321–330. [CrossRef]
78. Jackson, M.D.; Yoshida, S.; Muggeridge, A.H.; Johnson, H.D. Three-Dimensional Reservoir Characterization and Flow Simulation of Heterolithic Tidal Sandstones. *Am. Assoc. Pet. Geol. Bull.* **2005**, *89*, 507–528. [CrossRef]